Discovery of Active Hydrothermal Vent Fields Along the Central Indian Ridge, 8–12°S

Jonguk Kim[1] iD, **Seung-Kyu Son[1]** iD, **Dongsung Kim[2]**, **Sang-Joon Pak[1]**, **Ok Hwan Yu[2]** iD, **Sharon L. Walker[3]** iD, **Jihye Oh[1]** iD, **Sun Ki Choi[1]**, **Kongtae Ra[4]**, **Youngtak Ko[1]**, **Kyeong-Hong Kim[1]**, **Jun-Ho Lee[5]**, and **Juwon Son[6]**

[1]Deep-Sea Mineral Resources Research Center, Korea Institute of Ocean Science and Technology, Busan, South Korea, [2]Marine Ecosystem Research Center, Korea Institute of Ocean Science and Technology, Busan, South Korea, [3]National Oceanic and Atmospheric Administration/Pacific Marine Environmental Laboratory, Seattle, WA, USA, [4]Marine Environmental Research Center, Korea Institute of Ocean Science and Technology, Busan, South Korea, [5]Korean Seas Geosystem Research Unit, Korea Institute of Ocean Science and Technology, Busan, South Korea, [6]Marine Information Technology Corp, Seoul, South Korea

Abstract Four new hydrothermal vent fields were discovered on the slow spreading Central Indian Ridge (8–12°S; Segments 1–3), all located off-axis on abyssal hill structures or Ocean Core Complexes (OCCs). Each site was characterized using seafloor observation (towed camera system), plume chemistry (Fe, Mn, and CH_4; Conductivity, Temperature, and Depth sensor [CTD]/Miniature Autonomous Plume Recorder [MAPR]), and rock sampling (TVgrab/dredges). Different styles of venting on each segment reflect different geological settings, rock types, likely heat sources, and fluid pathways. The segment 1 field was located on the western flank of the axial valley at the base of OCC-1-1. High-temperature venting was inferred from plume characteristics and extensive seafloor sulfide mineralization, but only diffuse venting was observed. This site appears to be a magmatic-influenced basaltic-hosted system despite its off-axis location. Two low-temperature diffusely venting sites were located on abyssal hills 6 and 9 km off-axis on Segment 2. Plume particle, metal, and CH_4 concentrations were all very low, suggesting dilution of hydrothermal fluids by intrusion of seawater into the highly permeable flank area fault zone. The "Onnuri Vent Field" (OVF), located at the summit of OCC-3-2, vented clear, low-temperature fluids supporting abundant vent organisms (21 macrofaunal taxa). The plume particle signal was low to absent, but strong ORP anomalies correlated with high CH_4 and low metal concentrations. Sulfide mineralization was present, which suggests both serpentinization and magmatic/lithospheric influence on fluid composition. The detachment fault is the likely pathway for hydrothermal fluid circulation at this off-axis location. These new vent field discoveries, especially the OVF, contribute valuable information toward understanding Indian Ocean hydrothermal systems and their ecology/biogeography.

Plain Language Summary We discovered four new hydrothermal vent fields along the slow spreading Central Indian Ridge. The different styles of hydrothermal venting discovered at each site reflect the different geological settings, types of surrounding rocks, and likely heat sources driving the hydrothermal circulation. Among the new vent fields, the "Onnuri Vent Field" is particularly interesting because the isolated location, unique style of venting, and abundant vent biology provide valuable new information for understanding vent ecology and biogeography of the Indian Ocean.

1. Introduction

Deep sea hydrothermal venting, formed by circulation of hot fluid through crustal rocks at mid-ocean ridges and back-arc spreading centers, is one of the fundamental processes controlling the exchange of energy and matter between the interior of the Earth and the ocean. This process affects the composition of oceanic crust and ocean chemistry and provides energy sources for deep sea biological communities (Edmond et al., 1979; German & Seyfried, 2014; Humphris et al., 1995). Since first discovered in 1977, more than 500 confirmed and inferred active vent sites have been investigated throughout the global ocean in diverse volcanic and tectonic settings (Beaulieu et al., 2013, 2015). However, efforts to explore for and investigate hydrothermal vent sites have largely focused on the Pacific and Atlantic Oceans (German & Seyfried, 2014).

The Indian Ocean has mid-ocean spreading centers comprising 18,000 km length (28% of the global total) with various spreading rates, from ultraslow (Southwest Indian Ridge [SWIR], <12 mm/year) to slow and intermediate (Central Indian Ridge [CIR] and Southeast Indian Ridge (SEIR), 30–60 mm/year). Hydrothermal vent site frequency and characteristics are expected to vary in accordance with the diverse geological and tectonic features and variable spreading rates along the Indian Ocean Ridges (Baker & German, 2004; Beaulieu et al., 2015). Due to remote locations and inaccessibility, only five active hydrothermal fields have been identified so far: the Dodo vent field at 18°20′S, Solitaire field at 19°33′S (Nakamura et al., 2012), Edmond field at 23°52′S (Van Dover et al., 2001), and Kairei field at 25°19′S (Gamo et al., 2001) on the CIR and the Longqi field at 37°47′S (Tao et al., 2012) on the SWIR. Thus, the geological, geochemical, and biological features of hydrothermal systems along the Indian Ocean Ridges remain little known despite their potential role in understanding the global diversity of hydrothermal processes, including biodiversity and biogeography of vent species.

The four previously known hydrothermal vent fields on the southern CIR are located between the Marie Celeste Fracture Zone (MCFZ) and Rodrigues Triple Junction (RTJ) (18°S to 25°30′S). Although the CIR is a slow-to-intermediate spreading ridge, wide variations in fluid chemistry have been observed at CIR vent fields, suggesting diverse geological processes contribute to the formation of these hydrothermal vents (i.e., basaltic- and ultramafic-hosted hydrothermal systems), similar to the diversity of vent fields found along the slow spreading Mid-Atlantic Ridge (MAR) (Kumagai et al., 2008; Nakamura et al., 2012). More recently, several hydrothermal plume anomalies have been reported in the water column along the middle part of the CIR between 8°S and 17°S, where ridge morphology and tectonic structure (e.g., detachment faults and ocean core complexes [OCCs]) control increased plume incidence at ridge flank and rift wall locations (Pak et al., 2017; Son et al., 2014).

Here we present the results from the hydrothermal expedition by RV ISABU in 2018 that targeted select sites on Segments 1 through 3 (Pak et al., 2017) based on the previous plume-only surveys (Son et al., 2014). Four new active hydrothermal vent fields were located and characterized by seafloor observations, plume chemistry, and rock type. Despite their relative proximity within the same ridge system, all four of these new hydrothermal vent sites show diverse styles of venting, plume composition, and vent faunas, which can be attributed to different hydrothermal fluid formation conditions and transport pathways in the slow- to intermediate-rate spreading ridge setting. In addition, the vent fields in this region are located more than ~800 km north of previously known active vent fields (i.e., Dodo and Solitaire fields; Nakamura et al., 2012), and thus, our findings can provide further insights to understanding the isolated biogeographical provinces in the Indian Ocean.

2. Geological Setting and Hydrothermal Activity

The study area is located within the middle part of Central Indian Ridge (MCIR; 8–17°S), which shows typical morphology of slow spreading ridges (i.e., development of a 500–1,000 m-deep axial valley along the spreading center), marked by six first-order segments offset by six principle transform discontinuities. The inferred full spreading rates of the MCIR systematically increase from 27.6 to 40.9 mm/year from 8°S to 17°S, indicating a slow-to-moderate spreading ridge (Pak et al., 2017). These first-order segments vary from 36 to 281 km in length. The first-order segments are further subdivided into second-order segments by non-transform discontinuities (NTDs) with offset lengths ranging from 15 to 125 km. Of particular significance, these six segments of the MCIR feature 11 OCCs that mainly occur at inside corners of the segments, though some are perched in or near the NTDs (Pak et al., 2017). OCCs form due to the exhumation of mantle rocks through long-lived detachment faults (Tucholke et al., 1998). These detachment faults can become primary pathways for off-axis hydrothermal circulation (e.g., McCaig et al., 2007). OCCs are typically identified by corrugated dome-shaped structures and exposed deep-seated rock (i.e., serpentinite and/or gabbro or their equivalents). The area surveyed for this study included only the first three segments (Segments 1–3) from the north (Figure 1; Pak et al., 2017).

Segment 1 is bounded at the south by the Vema Fracture Zone (VFZ), which has the longest displacement (233 km) over the CIR. Segment 1 has a relatively narrow rift valley in the middle of the segment, ranging from 9 to 10 km in width and 3,700 to 3,800 m in depth. An OCC (OCC 1-1), located at the southern inside corner, shows two possible lineaments corresponding to breakaways. The older breakaway spreads ~30 km
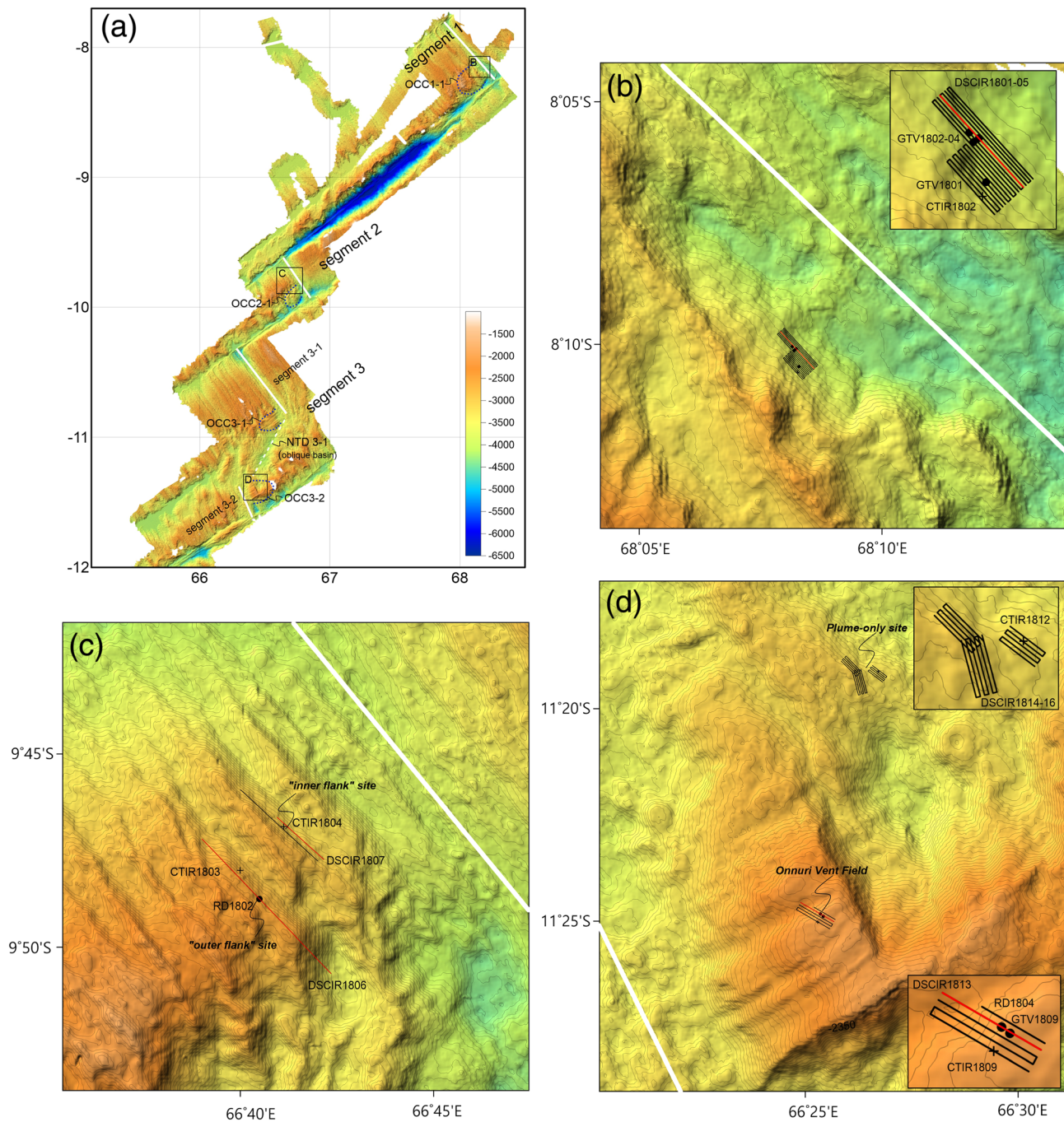
Figure 1. (a) Bathymetric map of Segments 1–3 on the Central Indian Ridge (CIR). Boxes in each segment show the area of hydrothermal activity and correspond to the maps shown in b–d. White lines indicate identified ridge axis. Blue-dotted lines at OCCs indicate the inferred boundaries of OCCs. (b–d) Detailed bathymetric maps of hydrothermally active areas on Segments 1–3 showing sampling locations. Insert maps show detailed sampling locations: Crosses, CTD hydrocasts (CTIR); dots, TV-grab (GTV) and rock dredge (RD); black lines show the camera tow tracklines (DSCIR). See Table S3 for detailed information of sampling locations. Route maps of representative camera tow tracks (red lines) are provided in Figures S1 to S4.

west of the axis, and the inferred younger breakaway is located 12 km west of the axial valley near the western flank (Figure 1; Pak et al., 2017).

Segment 2 is the shortest first-order segment of the MCIR. The middle stretch of Segment 2 is narrow and relatively shallow (11–13 km width, 3,800–3,900 m water depth) but becomes wider and deeper (~15 km width, 4,000–4,100 m water depth) at both tips. The northern and central part of the segment is
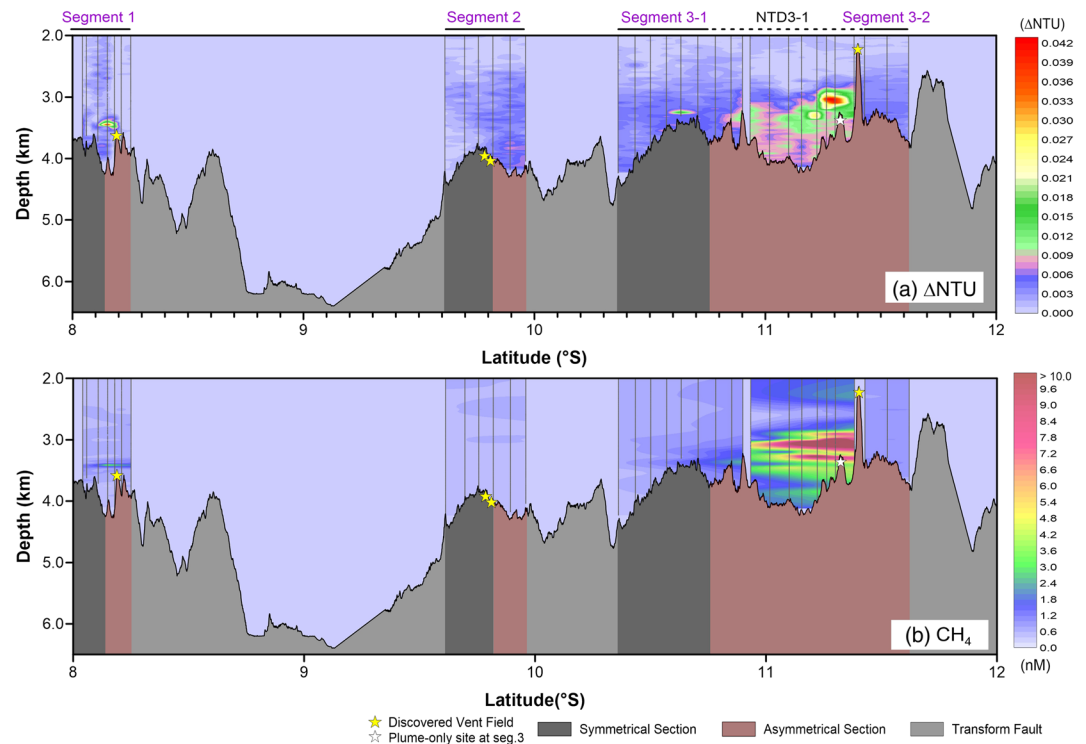
Figure 2. Contour plots showing (a) particle anomaly (ΔNTU) and (b) dissolved methane (CH$_4$, nM) along Segments 1–3 on the CIR (modified after Son et al., 2014). Yellow and white stars mark the locations of discovered vent fields and plume-only site, respectively. The bathymetric profile is color coded to identify symmetrical ridge sections (dark gray), asymmetrical ridge sections (reddish gray), and transform faults (light gray) according to seafloor morphology and tectonic structure.

characterized by typical abyssal hill fabric that is well developed on each flank, while the southwestern inside corner shows disturbed fabric due to formation of the OCC (OCC 2-1; Figure 1).

Segment 3 is bounded by a well-developed fracture zone at the north end of the segment where the axis is displaced right laterally by 109 km. This segment displays a totally different axial configuration due to the NTD between the two second-order segments (Figure 1). Second-order Segment 3-1 is ~67 km long with relatively well-developed abyssal hills, while Segment 3-2 is short (15 km long) and features poorly developed flank fabric. These second-order segments are separated by NTD 3-1, a 63 km-long and 18 km-wide oblique offset that deformed the preexisting abyssal hills of Segments 3-1 and 3-2. Two OCCs occur along Segment 3: OCC 3-1, located at the SW corner of Segment 3-1, and OCC 3-2 located at the NE flank of short Segment 3-2 (Figure 1). OCC 3-1 is similar to OCCs 1-1 and 2-1, which are also located at the southern inside corners of the respective segments. Although OCC 3-2 seems to be a remnant of a recessed segment, clear corrugation texture is observed on the inside slope (Pak et al., 2017).

Several hydrothermal plumes were identified by previous water column surveys along the three ridge segments that were the focus of the 2018 study area (Son et al., 2014). Clear hydrothermal plume anomalies observed on Segments 1 and 3 were identified by increased particulate and methane concentrations, and oxidation-reduction potential (ORP) anomalies. Only weak plume signals were detected on Segment 2 (Figure 2). Particulate anomalies that were well correlated with dissolved methane anomalies indicated plumes that were likely created by high-temperature sources (Son et al., 2014). The methane anomaly was highest in the southern part of Segment 3-2 (Segment 4 of Son et al., 2014), and suggested venting was associated with the exposure of ultramafic rock by deformation of oceanic crust near NTD 3-1 (Pak et al., 2017). The plume signals were generally accompanied by ORP anomalies, indicating proximity to active hydrothermal sources (Baker et al., 2016). Thus, these earlier results provided priority target sites for seafloor observations during the 2018 survey to locate hydrothermal vent sources.

3. Methods

3.1. Water Column Survey and Analyses of Plume Samples

The distribution of hydrothermal plumes in the study area was previously determined by systematic CTD/MAPR hydrocasts along the entire length of the MCIR between 8°S and 17°S (Son et al., 2014, Figure 2). Additional CTD/MAPR hydrocasts were completed during the 2018 survey to confirm ongoing activity at the identified sites and to collect water samples for measuring hydrothermal chemical tracers, including dissolved methane and trace metals (Fe and Mn). The CTD system (SeaBird, 911-*plus*) was equipped with a light transmissometer (Otronix, WetLabs C-star) and a 32-position rosette with 10 L Niskin bottles. Miniature Autonomous Plume Recorders (MAPRs) attached to the CTD package recorded optical backscattering and ORP every 5 s (about every 5 m at standard winch speed). The voltage output of the optical backscatter sensor (0–5 V) is equivalent to dimensionless nephelometric turbidity units (0–5 NTUs) (American Public Health Association, 1985), which are in turn highly correlated with typical deep sea particle mass concentration (Baker et al., 2001) and are reported here as the value greater than ambient nonplume water (ΔNTU). ORP is highly sensitive to short-lived reduced chemicals in hydrothermal plumes, such as Fe^{2+}, H_2S, Mn^{2+}, and H_2 (Walker et al., 2007). Due to hysteresis of the sensor, data are presented as either the time derivative (dE/dt, mV) or the magnitude of the overall decrease of a signal (ΔE, mV). Field experience shows that ORP anomalies are rarely found farther than ~1 km from their hydrothermal source (e.g., Baker et al., 2010; German et al., 2008).

Samples for dissolved methane analyses were transferred from the Niskin bottles into 100 ml brown-serum bottles to measure methane concentration. Methane concentrations were analyzed using a gas chromatograph/semiconductor detector (GC/SCD) according to the method suggested by Ohta et al. (1999). The detection limit of the method was estimated to be 0.2 nM.

Seawater samples for trace metal analysis were collected in preacid cleaned 500 ml LDPE bottles to prevent metal contamination on board. Unfiltered seawater samples for total dissolvable concentrations of trace metals (TDFe and TDMn) were acidified to a pH less than 2 by adding 0.7 ml of ultrapure grade of HNO_3. All samples were stored in plastic zip-loc storage bags at room temperature for on-land analysis. The samples were treated in a clean room container lab van to minimize metal contamination. Seawater samples for dissolved metal (DFe and DMn) analyses were immediately filtered using 0.45 µm polycarbonate membrane filters precleaned with high-purity nitric acid (ultragrade, Kanto chemical, Japan) and were acidified to a pH less than 2 by adding 0.7 ml of ultrapure grade of HNO_3. Mn and Fe concentrations in seawater samples were analyzed by using the seaFAST SP3 system (ESI, Elemental Scientific, Omaha, USA). The commercially available automated sample introduction and preconcentration system was used for seawater matrix separation; trace metal concentrations were determined by Inductively Coupled Plasma Mass Spectrometry (NexION 2000, Perkin Elmer Inc., USA). Accuracy of Mn and Fe measurement in seawater was determined using certified reference material for trace metals CASS-6 and NASS-7 (National Research Council of Canada) that were processed in the same way as the seawater samples. The recoveries ($N = 9$) of the measured Mn and Fe concentrations were 104% and 103% for CASS-6 and 107% and 104% for NASS-7 in this study.

Based on the analyzed data set of seawater samples, we calculated the Fe/Mn and CH_4/Mn ratios for each plume site. Only samples from the plume core depth were used to calculate the elemental ratios as suggested by Boulart et al. (2017).

3.2. Seafloor Observation and Rock Sampling

A total of 16 deep sea camera tows were conducted to identify hydrothermal vents, vent fauna, and massive sulfide deposits on the seafloor. The camera tow system comprised a main HD video camera, still camera, and video camcorder with a MAPR attached to provide temperature, pressure, optical backscatter, and ORP sensor data. Camera tow tracklines were selected based on the hydrothermal plume distribution data from previous work (Figures 1b–1d) (Pak et al., 2017; Son et al., 2014). The camera system was towed ~5–10 m above bottom at a ship speed of less than 0.5 knots.

Geological sampling was mainly performed with a TV-guided grab (TV grab) and a rock dredge. The targets for rock sampling were selected based on seafloor observations from the camera tows (Figures 1b–1d). Rock sampling by TV grab was available only at two hydrothermal vent sites on Segments 1 and 3 due to technical
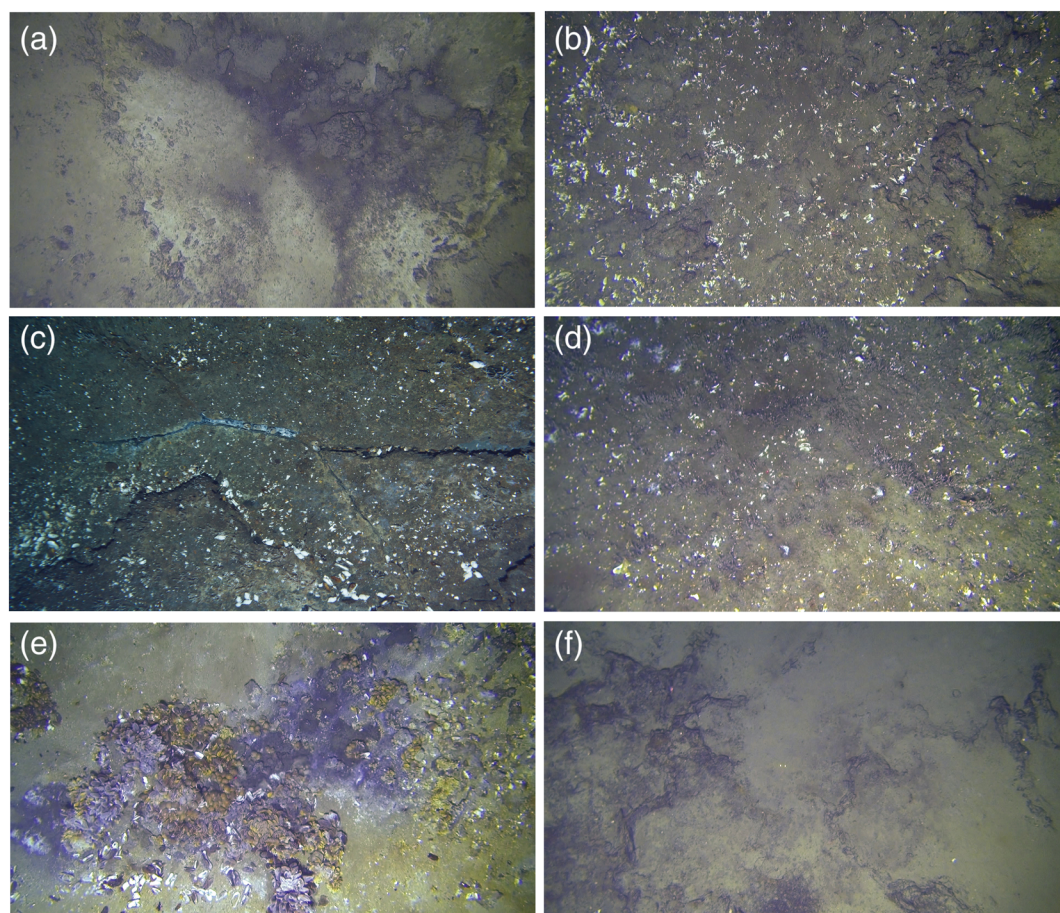
Figure 3. Photographs showing zonation of the active hydrothermal vent field (Onnuri Vent Field, OVF) on Segment 3. (a) Boundary of hydrothermal alteration zone with thin crust of Fe oxyhydroxide. (b) Occurrence of dead shells on hydrothermal alteration zone. (c) Fissure filled with vent fauna indicating possible diffuse flow. (d) Occurrence of living vent faunas with dead shells. (e) Clusters of various living vent fauna at the center of the hydrothermal vent field. (f) Alteration zone at the boundary of vent field (similar to a). Widths of photographs are ~6 m.

problems that arose during the cruise. At hydrothermal vent sites on Segment 2, rock dredging was carried out, and some altered rocks were collected.

3.3. Vent Fauna

Vent macrofauna were collected using a video-guided hydraulic grab (VGHG, Oktopus GmbH). Macrofauna were identified to family or genus level aboard ship as possible, preserved in 100% Ethanol and kept frozen at −80°C for further analysis. Cluster analyses and similarity profile (SIMPROF) permutation tests were carried out to categorize the macrofaunal similarity matrix between vent fields on the Indian Ocean Ridges, using a Sorensen's index based on presence/absence data and group-average linkage using the PRIMER 6.0 software package.

Sediment samples for nematode analysis were collected using a multiple corer (MC) and 3 acryl subcorers (Surface area, 10 cm^2). The samples were preserved in 5% formalin. In the laboratory, the nematodes were separated from the sediment by using Ludox HS40 colloidal silica (DuPont) with a specific gravity of 1.18 (Burgess, 2001). The nematodes were counted under a stereomicroscope and identified under an optical microscope to the lowest possible taxonomic level (Platt & Warwick, 1983, 1988; Warwick et al., 1998) using an Olympus BX51 microscope.

Table 1
Comparison of Plume Chemistry and Geological Setting of Hydrothermal Vent Fields Discovered in This Study

Vent field	Vent field on Segment 1	Outer site on Segment 2	Inner site on Segment 2	OVF on Segment 3	Plume-only site on Segment 3
Hydrocast	CTIR1802	CTIR1803	CTIR1804	CTIR1809	CTIR1812
			Plume chemistry		
Particle anomaly (max., ΔNTU)	0.118	0.006	0.005	0.002	0.011
ORP (min., dE/dt)	−0.41	−0.14	−0.062	−1.94	−1.1
TDFe (max., nM)	366	177[a]	—	191[a]	29
DFe (max., nM)	147	7.4	—	3.6	23
TDMn (max., nM)	46	2.9	—	1.5	5.9
DMn (max., nM)	46	2.5	—	1	6.1
CH4 (max., nM)	13.0	1.9	0.8	52.5	22.2
TDFe/TDMn (plume average)	8.64	—	—	—	5.41
DFe/DMn (plume average)	3.88	3.40	—	5.60	3.98
CH4/DMn (plume average)	0.30	0.66	—	36.2	4.28
			Geological settings and other properties		
Water depth	3,660–3,880 m	2,580–2,630 m	3,010–3,060 m	1990–2,170 m	2,990–3,070 m
Distance from spreading axis	~4 km	~9 km	~6 km	~11 km	
Basement rock type	Peridotite, Grabbro	Basalt	Basalt	Peridotite, Grabbro	Peridotite, Grabbro?
Mineral assemblage of vent field	Massive sulfides (Fe-rich, Cu-rich), Fe-oxides	amorphous silica, disseminated sulfides, Fe-oxides	no samples	Fe- and Mn- oxyhydroxides, disseminated sulfide	no sample
Vent fauna	non-vent animals	individual or small groups of vent fauna, dead shells	bacterial mat, crabs and dead shells	abundant vent fauna	non-vent animals

[a]The high total dissolvable Fe concentrations of samples from CTIR1803 and CTIR1809 sites are possibly due to contamination during processing and analyzing the samples.

4. Results

Four new active hydrothermal vent fields were discovered using the towed camera system for direct seafloor observations. None of the four vent fields were located directly on the spreading axis, and plumes from each segment had different physical and chemical properties. Two sites were associated with OCCs, and two others were located 6–9 km off-axis on abyssal hills. Among the four vent fields, the site located at the summit of OCC3-2 on Segment 3 had the most abundant vent fauna and was named the "Onnuri Vent Field" (OVF) (Figure 3). Geological settings and plume properties of the hydrothermal vent fields are summarized in Table 1.

4.1. Segment 1

The hydrothermal vent field on Segment 1 was located near 8°10.1′S and 68°08.2′E at depths ranging from 3,660 to 3,880 m on the western flank of the axial valley, in a topographic depression that was parallel to the spreading axis. It was estimated to be ~150–200 m in diameter based on camera observations. Rock samples from previous surveys show the basement rock is mainly composed of lower crust rock such as gabbro and minor amounts of serpentinized mantle peridotite (Yi et al., 2014), indicating this area comprises the base of the OCC at the southern inside corner of the ridge-transform fault intersection of segment 1 (OCC 1-1). Thus, hydrothermal activity on Segment 1 appears to be associated with the OCC structure. Seafloor images from the camera tow show outcrops of intensively jointed gabbroic blocks with variable sediment cover (Figure 4a). Exposure of the basement rock is mainly governed by topography (i.e., basement rock is more visible on steep slopes, cliffs, or within fissures).

Hydrothermal alteration can be identified by black, reddish brown, and yellow colored bottom sediment due to precipitation of Mn- and Fe-oxide and native sulfur. Several dead chimneys and sulfide mounds were
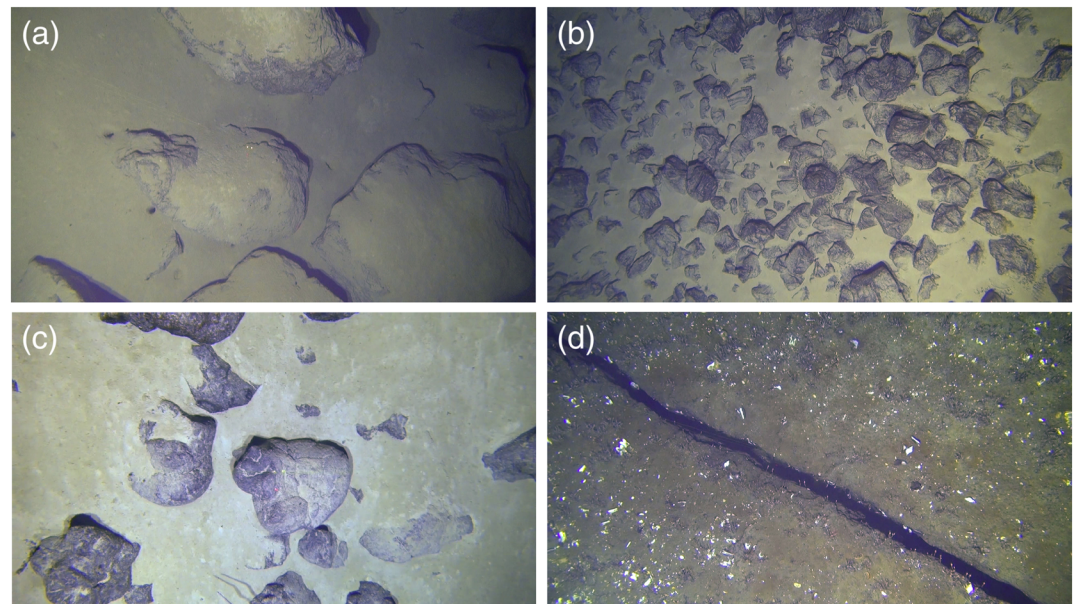
Figure 4. Photographs showing typical basement rock types at the four identified hydrothermal vent fields. (a) Massive gabbroic blocks covered by sediment on Segment 1. (b) Fragments of pillow lava covered by sediment at the 9 km off-axis site on Segment 2. (c) Occurrence of pillow lava covered by sediment at the 6 km off-axis site on Segment 2. (d) Massive substrate rock with fissure in the OVF at the summit of OCC 3-2 on Segment 3. Widths of photographs are ~6 m.

observed but discontinuously exposed on the sediment-covered slope within the alteration zone (Figure S1 in the supporting information). The overall appearance of hydrothermal precipitates and absence of vent fauna suggested that the vent field on Segment 1 was waning; however, observation of shimmering fluids on some chimneys and ORP anomalies ($\Delta E \sim -25$ to -50 mV) during the camera tow demonstrates that diffuse hydrothermal fluid flow is present throughout the area (Figure 5b). The robust above-bottom plume (described below) at this site suggests high-temperature venting was nearby, though not directly observed.

Various types of sulfide were recovered by several TV grab operations (GTV1801 to GTV1804; Figure 1). Samples from GTV1801 were characterized by pyrite-dominant massive sulfides. Fragments of hydrothermal chimneys of Cu-rich sulfides were also collected. Other rock samples were sulfides, Fe-oxides-rich fragments, and altered ores with greenish secondary Cu-bearing minerals (Figure 6). The massive sulfides imply that this sampling site corresponds to a hydrothermal mound that previously hosted more robust high-temperature venting.

Figure 7 presents the water column profiles of optical backscatter (ΔNTU), percent light transmission, ORP (as dE/dt), total dissolvable and dissolved Fe and Mn concentrations, and dissolved methane concentrations at each vent field, together with one plume-only site (CTIR1812) in Segment 3. Hydrocast CTIR1802 was located on Segment 1 within the area where several inactive chimney structures were observed during the camera tow (Figure 1). Increased turbidity was observed in the water column from 3,300 m to the seafloor (a rise height of ~400 m), with prominent above-bottom maxima at 3,380, 3,450, and 3,620 m. Maximum ΔNTU values over this site (>0.12 during camera lowerings) were the most intense observed during this expedition. Each turbidity peak was accompanied by a decrease in ORP value ($\Delta E \sim -8$ mV) and increased concentration of Fe, Mn (total dissolvable and dissolved), and dissolved methane. Both TDFe and DFe concentrations are elevated at plume depths (DFe up to 147 nM and DMn up to 46 nM). The much higher concentrations of TDFe compared to DFe indicate most of the Fe is in the particulate phase. On the other hand, there is little difference between TDMn and DMn concentrations, indicating most of the Mn remains in solution. The high concentrations of DFe and DMn also point to high-temperature venting at this vent field, even though only diffuse venting was observed during the camera tows. The multilayered above-bottom plume suggests the vent field comprises multiple sources of both focused high-temperature and diffuse
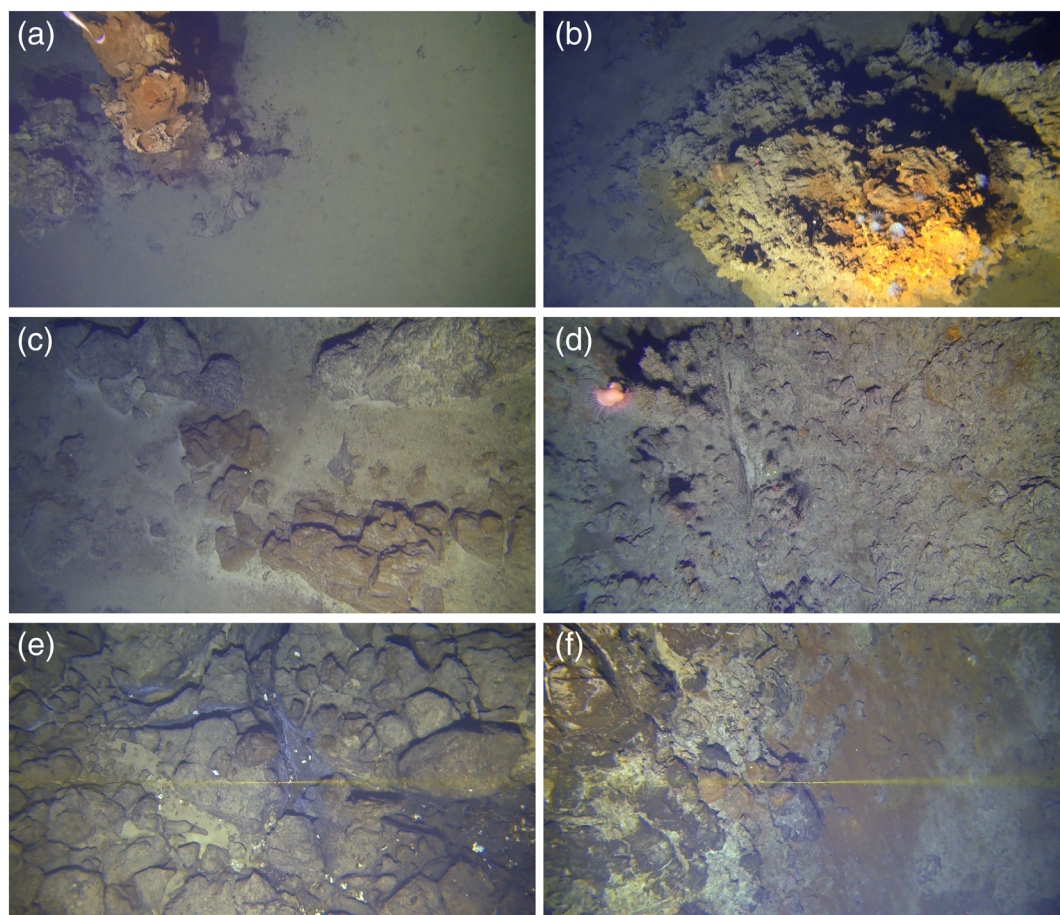
Figure 5. Photographs from hydrothermal vent fields on Segments 1 and 2. (a) Inactive chimney on Segment 1. (b) Diffuse vent on Segment 1. (c) Broken chimney at the 9 km off-axis (outer flank) site on Segment 2. (d) Massive inactive chimney zone at the 9 km off-axis (outer flank) site on Segment 2. (e) Bacterial mat and dead shells with altered rock boulders at the 6 km off-axis (inner flank) site on Segment 2. (f) Alteration zone with dead chimneys at the 6 km off-axis (inner flank) site on Segment 2. Widths of photographs are ~6 m.

low-temperature venting. Because this site sits on the steep inward-facing slope of OCC 1-1, it is also possible that additional sources may be located further upslope or downslope of the camera tow survey area.

4.2. Segment 2

Active venting was expected on Segment 2 based on ORP anomalies observed during previous work, although particle and methane anomalies were weak (Son et al., 2014). ORP anomalies were mapped more thoroughly during CTD tows in 2018, and two off-axis abyssal hill locations near 9°47.5′S, 66°41.9′E (~6 km west of the axis) and 9°48.9′S, 66°40.6′E (~9 km west of the axis) were identified as the likely source locations. Camera tow lines were aligned parallel to the spreading center at each of these sites (Figure 1).

The basement rock exposed on the seafloor was mainly composed of basaltic pillow lavas (Figures 4b and 4c), indicating typical abyssal hill structure as inferred by the symmetrical ridge morphology at this point in the segment (Pak et al., 2017). Similar to Segment 1, the majority of seafloor is covered by fine-grained sediment of variable thickness. Ripple marks on some surface sediments indicate relatively strong bottom currents can occur in this region.

Active hydrothermal vent fields were identified at each site. The 9 km off-axis "outer flank" site was found at water depths of 2,580–2,630 m, while the 6 km off-axis "inner flank" site was about 400 m deeper at 3,010–3,060 m water depth. The outer flank site was defined by an alteration zone that continued for ~300 m along the camera tow track line (Figures 5c and 5d). A significant ORP anomaly ($\Delta E = -56$ mV) indicated
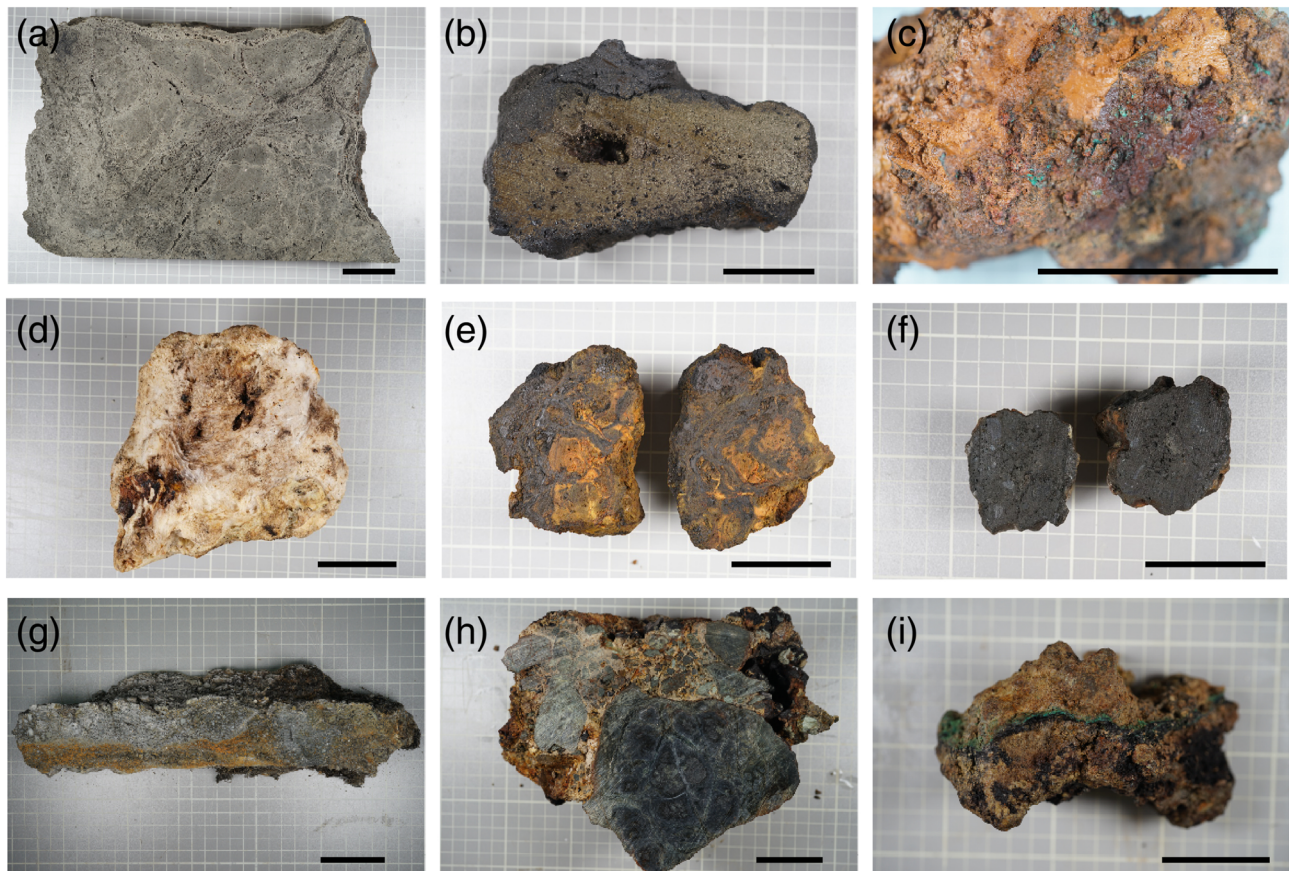
Figure 6. Photographs of various types of hydrothermal precipitates and altered rocks collected from the hydrothermal vent fields on Segments 1–3. (a) Pyrite-dominant massive sulfide (segment 1). (b) Cu-rich sulfide (Segment 1). (c) Fe-oxyhydroxides fragment with secondary Cu-mineral (green color) (Segment 1). (d) Filamentous textured amorphous silica fragment (Segment 2). (e) Hydrothermally altered Mn-Si dominant fragment (Segment 2). (f) Altered basalt fragment with fine grained sulfide precipitation (Segment 2). (g) Barite-rich hydrothermal precipitates with disseminated sulfides (OVF on Segment 3). (h) Hydrothermally altered breccia influenced by serpentinization (OVF). (i) Crust-type hydrothermal precipitates with secondary Cu mineral (OVF). Scale bars are 5 cm.

hydrothermal discharge was active within the alteration zone (DSCIR1806; Figures 1 and S2). Variously sized broken chimneys, thick massive sulfide and Fe oxide-hydroxide crust, and yellowish to brown colored precipitates or bacterial mat were observed throughout the area (Figures 5c–5f). Although no large clusters of vent macrofauna were observed, vent animals were seen occasionally as individual or small groups (Figure S2).

The inner flank vent field was identified during camera tow (DSCIR1807; Figures 1 and S3). This vent field was characterized by diffuse flow (indicated by ORP anomalies of $\Delta E \sim -5$ to 20 mV) along fissures or cracks between pillow lavas and the presence of inactive chimneys and sulfide mounds. Bacterial mat occurred along a lava fissure at the boundary of the vent field, and crabs and dead shells were found near the diffuse flow zone.

Mineralized samples were collected by a rock dredge at the 9 km off-axis "outer flank" site. Samples were mainly reddish-tinted filamentous fragments of amorphous silica (Figure 6), indicative of high-Si hydrothermal mineralization at this site. Other samples collected were rock fragments bearing sulfides, Fe-oxides, and low-temperature amorphous silica aggregates.

Plume signals observed at the two off-axis sites on Segment 2 were characterized by weak above-bottom particle ($\Delta NTU = 0.005$ to 0.006) and ORP anomalies ($\Delta E < -2$ mV), along with low DFe, DMn, and methane concentrations (Figure 7). CTIR1803 was located over outer flank site at a depth of 2,670 m. The turbidity and ORP anomalies occurred below 2,370 m in the water column and correlated with increases of DFe
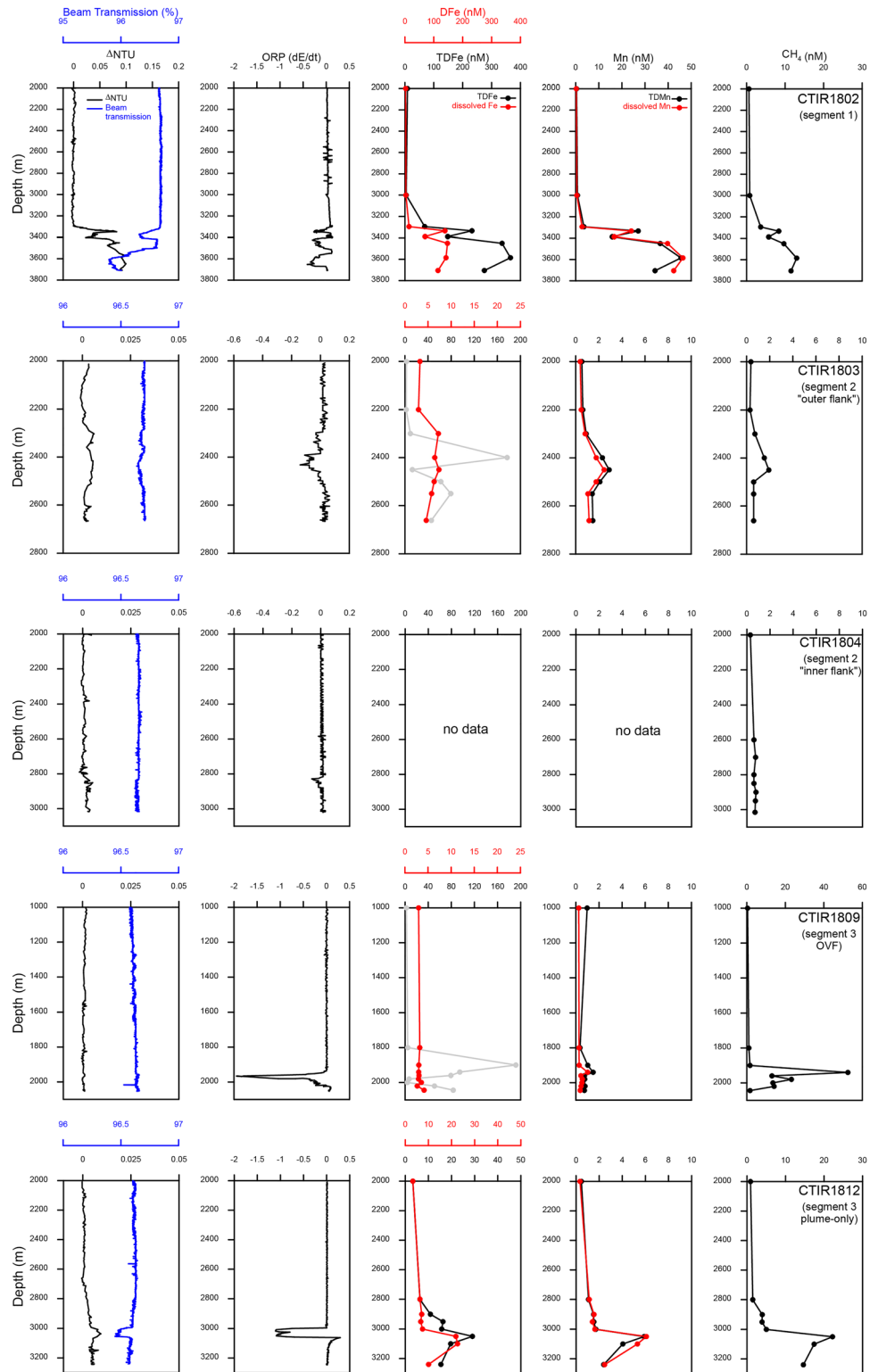
Figure 7. Water column profiles of beam transmission, optical backscattering anomaly (ΔNTU), time derivative of oxidation-reduction potential (dE/dt, mV), total dissolvable and dissolved Fe, total dissolvable and dissolved Mn, and dissolved methane from the CTD/MAPR hydrocasts at the four identified hydrothermal vent fields on Segments 1–3 and one plume-only site on Segment 3 (CTIR1812). Note that different ranges are applied to X axes in some plots for data presentation. The high concentrations of TDFe data for samples from CTIR1803 and 1809 are due to possible contamination (plotted in gray).

(up to 7 nM), DMn (up to 3 nM) and methane (up to 2 nM). Plume maximum values showed a rise height ~200 m above the seafloor. TDFe concentrations up to 177 nM suggested a high percentage of TDFe was in the particulate phase given the low DFe values, but that was inconsistent with the weak particle anomaly. Based on comparison with other TDFe and DFe profiles (i.e., CTIR1802 and CTIR1812) where TDFe and DFe had more similar distribution patterns, the possibility of contamination during processing and analyzing the samples cannot be ruled out for TDFe in CTIR1803.

CTIR1804 was located closer to the spreading axis over the inner flank site. Similar to cast CTIR 1803, only weak turbidity and ORP anomalies were detected ~200 m above the seafloor (Figure 7). ORP is a highly sensitive proxy for hydrothermal venting, especially for detecting particle-poor low-temperature diffuse vents (Baker et al., 2016). The weak plume signal was consistent with observations of only bacterial mat, dead shells, and weak diffuse flow (detectable only by ORP anomalies near the seafloor) in this region.

4.3. Segment 3

Along Segment 3, including the extended NTD (3-1), significant plume anomalies were detected in previous works (Figure 2, Son et al., 2014). Although a particle plume signal (ΔNTU) was observed along the spreading axis of Segment 3-1 (i.e., near 10°40′S in Figure 2), no hydrothermal alteration or hydrothermal precipitates were observed during camera tows in 2018. In addition, no vent field was found during the camera tows at the site of plume signals near 11°20′S, 66°26′E at the southern end of the extended offset where the plume signature (ΔNTU) was most intensive during the previous surveys (Son et al., 2014). Although no vent field was identified, hydrocast CTIR1812 was completed at 11°19.1′S, 66°26.7′E near the site of highest plume signal seen by Son et al. (2014), and a plume was still present in a thin, but well-defined, layer between 2,990 and 3,070 m water depth (~170 m above bottom) (Figure 7). The decrease in light transmission (maximum ΔNTU = 0.01) was accompanied by a significant ORP anomaly (ΔE ~ −20 mV), and water samples were characterized by elevated DFe and TDFe (up to 29 nM), TDMn (up to 6 nM), and high dissolved methane (up to 22 nM), suggesting the possibility that high-temperature venting at this site remains to be identified by future work.

The active hydrothermal vent field (OVF) was discovered ~11 km off-axis near the summit of OCC 3-2 at 11°24.9′S, 66°25.4′E at 1,990–2,170 m water depth, where a methane-only anomaly was detected in the previous surveys (i.e., Son et al., 2014, Figure 2). Around the OVF, small chimneys, altered rocks, and Fe-oxide crust were widely distributed in an area approximately 100–150 m diameter. Abundant vent organisms, including hairy snails, mussels, barnacles, shrimps, and crabs formed several clusters within the vent field (Figure 3). The OVF showed typical zonation from the outer alteration zone with Fe-oxide crust to a diffuse zone with abundant dead shells, and the active zone with living fauna in the middle of vent field (Figures 3 and S4). Clear fluid was noticeably venting among clusters of dead shells and living fauna, producing intense ORP anomalies (ΔE > −150 mV). The fluid usually effused out from the fissures of basement rock fissures, and no typical chimney structures were observed.

Mineralized samples collected by TV grab at the OVF (Segment 3 OCC 3-2) were disseminated sulfide assemblages (Figure 6) with barite precipitated in the outer zones of the samples. Sulfides and Fe- and Mn-oxyhydroxides were precipitated along the joints of brecciated rock fragments. Samples collected by rock dredges were mainly breccia-type sulfides and fragments of serpentinized mantle rocks. Some breccia-type sulfides displayed thin greenish layers of Cu-bearing secondary minerals. Occurrence of secondary Cu minerals implies that (1) the hydrothermal system might be affected by high-temperature fluids at least beneath the site although plume data indicate low-temperature, diffuse venting is dominant or (2) high-temperature venting was present in the past but the site is now waning.

The plume over the OVF site (CTIR1809; Figure 7) was particle-poor (max. ΔNTU = 0.002) but characterized by a significant ORP anomaly (ΔE = −20 mV) ~ 100 m above the bottom (1,940–2,030 m depth interval), with corresponding increases in DFe, DMn, and methane. The dissolved methane concentration at this site (up to 53 nM) was the highest of all plume sites sampled during this study. The OVF is located at the summit of OCC 3-2, and thus, the high methane concentration suggests that serpentinization of the ultramafic rocks comprising the OVF basement influences fluid composition. The location of OVF appears to be the source of one of the shallow, methane only "hydrochemical" plumes detected near the massifs along the MCIR by Son et al. (2014). It is important to note that similar to CTIR1803 (Segment 2), cast CTIR1809 had unusually high
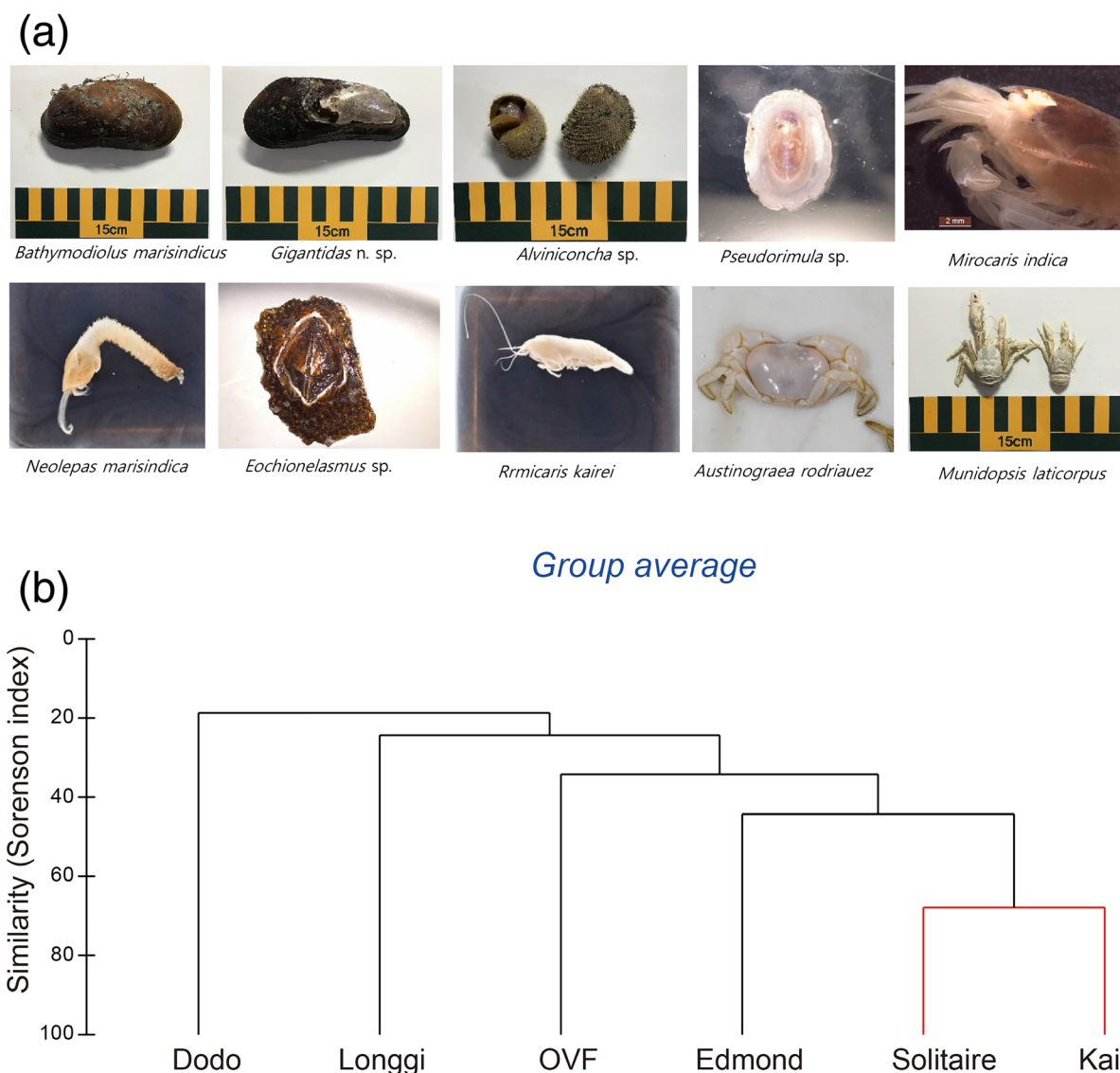
(a)

Bathymodiolus marisindicus   *Gigantidas* n. sp.   *Alviniconcha* sp.   *Pseudorimula* sp.   *Mirocaris indica*

Neolepas marisindica   *Eochionelasmus* sp.   *Rrmicaris kairei*   *Austinograea rodriauez*   *Munidopsis laticorpus*

(b)

Group average

Figure 8. (a) Photographs of dominant (>2% of total occurrence) macrofauna collected from the OVF (upper panel). (b) Clustering analysis using group-average linkage for presence/absence records of hydrothermal vent animals across six vent fields in the Indian Ocean (lower panel). Connected red lines indicate the same group by SIMPER analysis ($p < 0.05$). Presence/absence data for hydrothermal vent animals at five vent fields complied from Copley et al. (2016).

concentrations of TDFe in samples from the plume depth yet very low DFe concentration, implying a high percentage of TDFe should be in the particulate phase. This result is inconsistent with the absence of turbidity and the observation of clear fluids venting at OVF, which suggest that Fe would more likely be in the dissolved phase. Therefore, as with CTIR1803, we cannot rule out contamination during processing or analyzing this sample.

We identified 21 macrofaunal taxa in samples collected from the OVF (Table S1). The macrofauna are visually dominated by the mussels *Bathymodiolus marisindicus* (31.1%) and *Bathymodiolus* sp.1 (10%), and the stalked barnacle *Neolepas marisindica* (24.2%) (Figure 8). Six species, *Gigantidas* n. sp., *Alvinocaris markensis*, *Paralepetopsis ferrugivora*, *Lepetodirilus* sp. C, *Nereis* sp., and *Branchipolynoe seepensis* are not known in other known vent fields in the Indian Ocean. Three species were previously known to appear in only one other vent field (i.e., *Archinome* sp. indet. Edmond in the Edmond field [CIR], *Branchipolynoe* spp. CIR in the Kairei field [CIR], and *Hesiolyra cf. bergi* in the Longqi field [SWIR]). Among the 21 species at the OVF, 14 species are known to appear at active vent fields on the CIR, while six species are found at the Longqi vent field on the SWIR (Table S1).

In total, 65 nematodes appeared at the OVF, which consisted of 2 classes, 7 orders, 12 families, and 24 genera (Table S2). Genera of nematodes with the highest density were *Halalaimus* spp. (nine individuals) and *Cobbia* spp. (seven individuals), and there were 11 genera with two to six individuals (*Paralongicyatholaimus* spp., *Richtersia* spp., *Aponema* spp., *Molgolaimus* spp., *Daptonema* spp., *Linhystera* spp., *Desmoscolex* spp., *Araeolaimus* spp., *Pselionema* spp., *Oxystomina* spp., and *Wieseria* spp.). *Halalaimus* spp. was the dominant genus at the OVF (13.8% of individuals). *Cobbia* spp. was the second most abundant genera (10.8% of individuals), and both these genera were more than 10% of the total nematode density. There were eight genera with a density of only one individual (*Cyatholaimus* spp., *Bolbolaimus* spp., *Spirinia* spp., *Gnomoxyala* spp., *Southerniella* spp., *Filoncholaimus* spp., *Adoncholaimus* spp., and *Enoplolaimus* spp.).

The most abundant families of nematodes were Xyalidae and Oxystominidae. Xyalidae was the dominant family at the OVF (23.1% of individuals), and Oxystominidae was the second most dominant (21.5% of individuals). These two families accounted for about 45% of all specimens at the OVF.

5. Discussion

5.1. Diverse Locations of the Hydrothermal Vent Fields

On medium and fast spreading ridges, hydrothermal plume incidence is generally related to spreading rate and the presence of axial magma chambers (Baker, 2009). Active vents tend to be located within relatively narrow along-axis neovolcanic zones at segment topographic highs (Baker & German, 2004). Slow spreading ridges are more complex geological settings characterized by broad, deep axial valleys; a variety of axial offset types; and detachment faults leading to more diverse vent locations (Fouquet et al., 2010; German et al., 2010). For example, along the MAR, hydrothermal vents have been identified on neovolcanic axial ridges (Snake Pit, Gente et al., 1991; Lucky Strike, Fouquet et al., 1995), at the intersection of axial valley faults (TAG, Rona et al., 1986), on valley walls (Logatchev, Bogdanov et al., 1995; Moytirra, Wheeler et al., 2013), at NTDs (Rainbow, Charlou et al., 2002), and entirely outside the axial valley (Lost City, Kelley et al., 2005; Nibelungen, Melchert et al., 2008). MAR hydrothermal vent fields also occur in association with different rock types including basaltic-hosted sites (Snake Pit and Lucky Strike), mixed influence sites of mafic and ultramafic rocks (Rainbow, Logatchev, TAG, and Nibelungen), and purely ultramafic systems (Lost City), reflecting their locations at complex ridge settings.

The CIR, with spreading rates ranging from slow to intermediate, has morphological features similar to slow spreading ridges. The four previously known hydrothermal vent fields identified along the CIR include both basaltic-hosted systems (Dodo, Solitaire, and Edmond) and an ultramafic-hosted system (Kairei) (Kawagucci et al., 2016; Okino et al., 2015). The newly identified (by this study) hydrothermal vent fields occupy different morphological settings at each segment (Figure 9). The hydrothermal vent field on Segment 1 is located on the wall of a depression on the west flank of the axial valley associated with an OCC (Figure 9a). Occurrence of gabbroic blocks observed near the vent field and sampling of gabbroic and serpentinized peridotite at this site indicate the hydrothermal activity might be influenced by ultramafic rocks. However, the location of the vent field, which is relatively close to the ridge axis, suggests a mixed influence of mafic and ultramafic host rock on the formation of this hydrothermal system.

The two vent fields discovered on the ridge flanks of Segment 2 are located on typical abyssal hill structures of a symmetrical ridge section (Figure 9b). Basaltic pillow lavas observed near these vent fields support that they are basaltic-hosted hydrothermal systems, although both sites are located outside of the axial valley. Vent sites on Segment 2 had weak plume signals, but OPR, Fe, Mn, and CH_4 all indicated venting was still active. Active low-temperature, diffuse venting was confirmed by the occurrence of near-bottom ORP anomalies, bacterial mat, shells, and hydrothermal precipitates typical of low temperature formation such as Fe-oxides and amorphous silica. As both sites were away from the neo-volcanic zone (i.e., magmatic heat source), such diffuse venting may result from mixing of high-temperature fluids with downwelling seawater via the highly permeable fault zone of the ridge flank area. Diffuse venting is expected to be common along ridge crests and on ridge flanks, and the presence of off-axis vent fields as far as 9 km distant from the ridge axis of Segment 2 suggests that widespread diffuse flow on ridge flanks would has been underestimated. Observation of variously sized broken chimneys and possible massive sulfide mounds implies formation
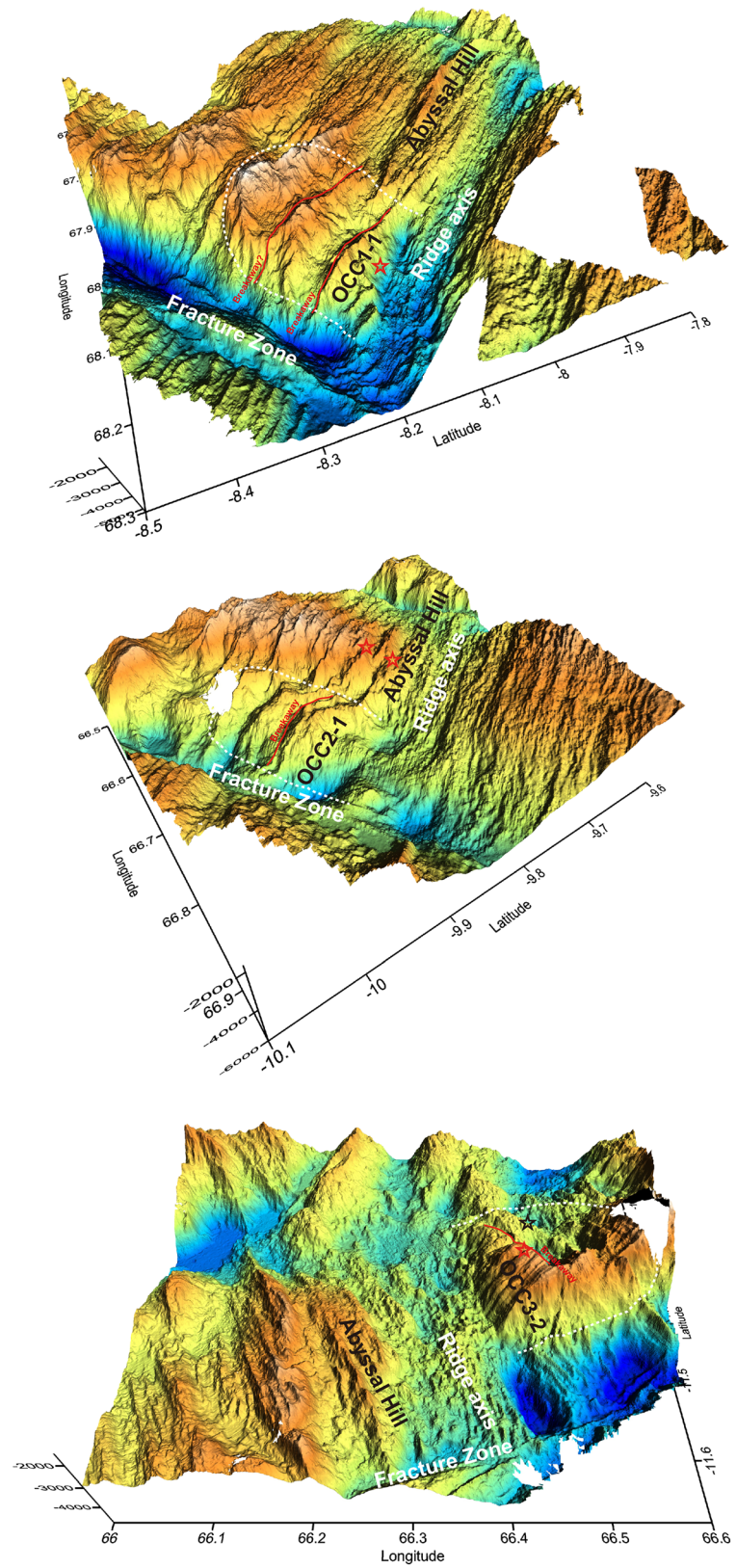
Figure 9. Three-dimensional perspective views of the hydrothermal vent fields discovered on Segments 1–3 (a–c, respectively). Locations of hydrothermal vent fields are marked with red stars. Plume-only site on Segment 3 is marked with black star. White dotted lines and red lines indicate inferred boundary of OCC and breakaway, respectively.

by high-temperature venting in the past. More sampling is required to understand the history of these off-axis vent fields.

Among the vent fields identified by this study, the OVF, an active vent field with abundant vent fauna, occurred at a distinctive location situated at the summit of OCC 3-2, at a distance of ~11 km from the axial neo-volcanic zone and a shallower depth (~2,000 m) than the other sites (Figure 9c). Only gabbroic and ultramafic rocks were collected during rock sampling by TV grab and dredges. The lack of particulates in the plume, along with high methane with negligible dissolved metals concentrations, suggests that the OVF is an ultramafic-hosted hydrothermal system driven by the heat of serpentinization reactions. However, precipitation of disseminated Cu, Fe, and Zn sulfides with silica in the vent field suggests that the hydrothermal fluids are not formed solely by serpentinization but require other heat sources and water-rock interactions as well.

Overall, the location and style of the OVF appear to be similar to the Von Damm Vent Field (VDVF) on the Mid-Cayman Spreading Center, which is located at a shallow depth of 2,280 m on the upper slope of an OCC (Connelly et al., 2012; Hodgkinson et al., 2015). Hodgkinson et al. (2015) proposed that hydrothermal circulation driven by residual heat from uplifted lower crust and upper mantle can explain the particle-poor hydrothermal plume, intermediate temperature, and low concentration of dissolved metals in the vent fluid of the VDVF. More recently, Harding et al. (2017) showed a low seismic velocity anomaly below the VDVF and argued that the heat source driving venting is either magmatic sill intrusion or lithospheric heat, which may also be possible heat source(s) at the OVF.

5.2. Chemical Compositions of the Hydrothermal Plumes at Different Locations

The diverse styles of hydrothermal venting along the CIR, as expressed by fluid composition, especially elemental ratios such as Fe/Mn and CH_4/Mn, reflect the differing rock compositions and vent site locations (relative to the spreading axis). Fe and Mn are two of the most enriched metals in hydrothermal fluids. However, they show different behavior upon mixing with seawater. Particulate Fe is formed mainly by precipitation of sulfide phases and Fe-oxyhydroxides, which removes up to 50% of the total dissolved Fe (German & Seyfried, 2014). Unlike Fe, Mn remains predominantly dissolved in the nonbuoyant plume and thus can be transported long distances. Fe/Mn of high-temperature hydrothermal fluids and plumes typically ranges between 1 and 7 in mid-ocean ridge systems (Baker et al., 2002; Von Damm, 1990), while low Fe/Mn values (<1) are generally found in lower-temperature hydrothermal fluids and diffuse vents, a result of selective removal of Fe in the subseafloor.

The plumes over these four newly discovered vent sites had DFe/DMn values of 3.40 to 5.60, within the typical range of mid-ocean ridge hydrothermal system (Figure 10). TDFe/TDMn values (8.64 and 5.41) of CTIR1802 and CTIR1812 were higher than DFe/DMn (3.88 and 3.98) in the same plume samples and were attributed to the majority of Fe in the plume being in the particulate phase (i.e., as Fe-sulfide and/or Fe-oxyhydroxide particles) (Table 1). Differences in DFe/DMn among the four vent fields were insignificant. Although the OVF had a slightly higher DFe/DMn ratio (5.60), DFe and DMn concentrations were 1–2 orders lower than at the other vent fields (Figure 10). Low concentration of DMn in plume water at the OVF cannot be attributed to sulfide precipitation in the subseafloor. Rather, vapor enrichment by subsurface boiling of fluids is a more plausible process for high dissolved methane paired with low DFe and DMn concentrations. Alternatively, high metal concentrations are not expected from a site associated with serpentinization.

CH_4/DMn ratios in the hydrothermal plumes varied from 0.30 (Segment 1) to 36.2 (OVF, Segment 3), suggesting different types of hydrothermal venting (Table 1). Ultramafic hosted hydrothermal systems have high concentrations of CH_4 and H_2 resulting from serpentinization reactions during the circulation of water through ultramafic rocks (Charlou et al., 2002). The high CH_4/DMn in plumes at the OVF (36.2) and CTIR1812 (4.28) on Segment 3 coincides with their location on ultramafic massifs.

Although the vent field on Segment 1 was located on the slope of an OCC, the low CH_4/DMn values were similar to those of basaltic-hosted hydrothermal systems (Figure 10). The high particle anomaly along with high TDFe and TDMn concentrations indicates high-temperature hydrothermal activity was present on Segment 1, even though it was not directly observed. The Segment 1 vent field was located within the rift valley, close to the ridge axis (<4 km), so an axial magma chamber or other intruded hot basaltic rock might be a plausible heat source in addition to hot gabbroic pluton (McCaig et al., 2007). If hydrothermal fluids are
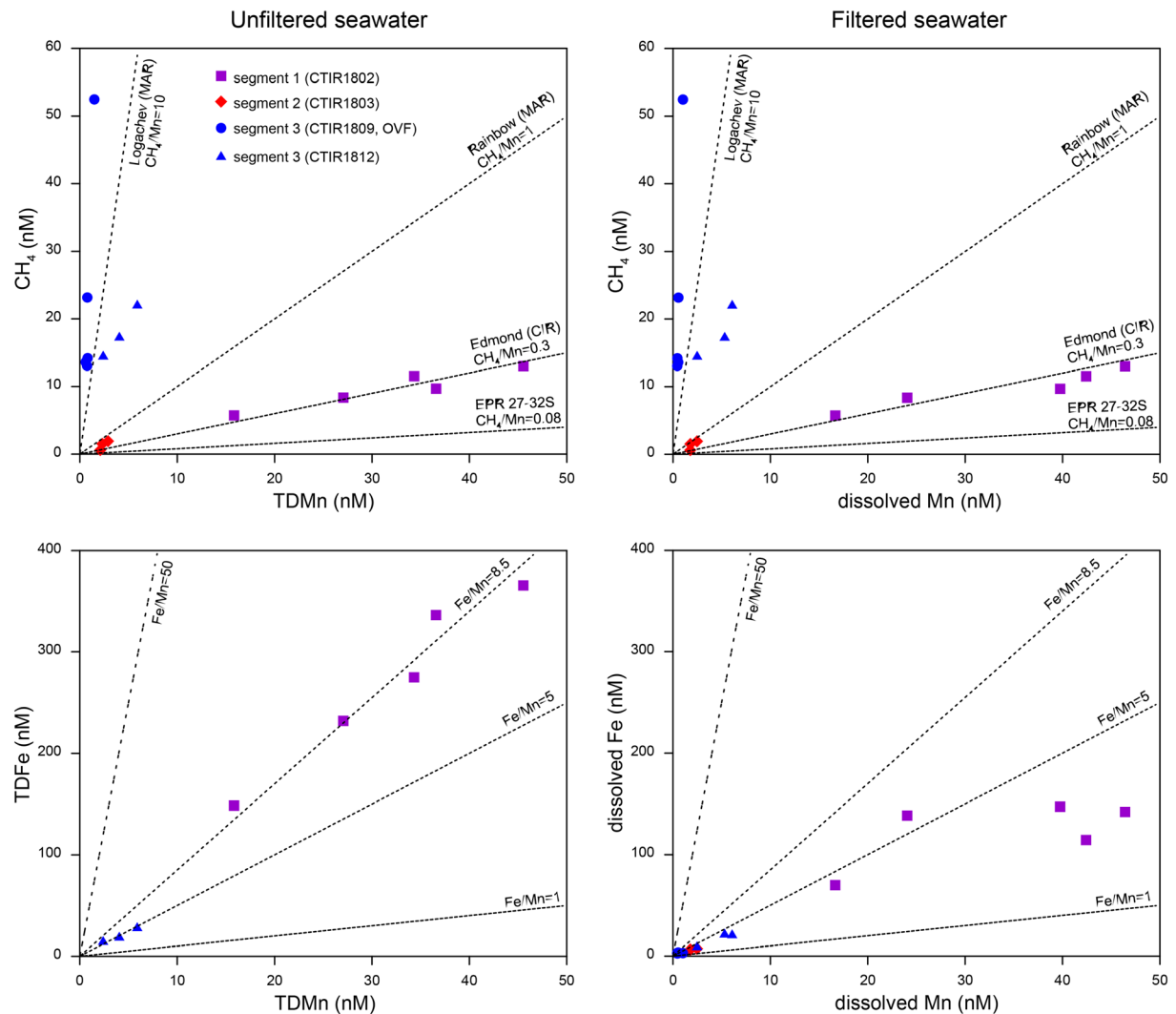
Figure 10. Chemical analyses of water samples from CTIR1802, CTIR1803, CTIR1809, and CTIR1812. (a) Dissolved CH_4 versus TDMn concentrations. (b) Dissolved CH_4 versus DMn concentrations. (c) TDFe versus TDMn concentrations. (d) DFe versus DMn concentrations. Only samples from the plume core depth were used for the plots. TDFe data for samples from CTIR1803 and CTIR1809 are not included due to possible contamination. The dashed lines in dissolved CH_4 versus Mn concentrations show the trends for Rainbow (MAR) (Charlou et al., 2002), Logachev (MAR) (Schmidt et al., 2007), Edmond (CIR) (Gallant and Von Damm), and EPR 23–32°S (Gharib et al., 2005) vent fields.

heated by basaltic magma and discharged through a highly permeable fault zone without significant interaction with peridotite beneath the fault zone, the composition might be inherited more from basaltic host rock than from the ultramafic rocks, as McCaig et al. (2007) proposed for the formation of TAG-type vents.

Plume samples from the vent field identified on Segment 2 had CH_4/DMn of 0.66, which was similar but slightly higher than that for basaltic-hosted sites on the EPR or CIR (Kawagucci et al., 2008, 2016). Some methane input processes, such as deep penetration of hydrothermal fluids to gabbroic intrusion, high volatile degassing, microbial methanogenesis, and thermal decomposition of organic carbon, can be considered for the apparent high CH_4/Mn ratios. Considering the low concentration of CH_4 at the site, however, methane input to the Segment 2 site appears to be relatively insignificant.

5.3. Vent Fauna of the OVF

Vent fauna of the Central Indian Ocean are known to define one of the six main biogeographical provinces of the global mid-ocean ridge system (Shank, 2004; Van Dover et al., 2002). The Indian Ocean has been suggested as a corridor for dispersal of vent animals between the Atlantic and Pacific oceans (German

et al., 1998). Desbruyères et al. (2007) proposed a potential past dispersal pathway via the SEIR, Macquarie Ridge, and Kemadec Arc to explain a relatively close connection between the western Pacific back-arc and CIR vent fauna. A recent study on stalked barnacles collected from the Kairei and Solitaire vent fields, however, provided molecular phylogeographic evidence against the "corridor" hypothesis and suggested that the vent fauna migrated from the Pacific Ocean to the Indian Ocean through the Southern Ocean (Watanabe et al., 2018). Considering the limited number of well-studied active vent fields in the Indian Ocean (Kairei, Edmond, Solitaire, and Dodo on the CIR and Longqui on the SWIR), compared to >250 active vent fields worldwide (Beaulieu et al., 2013), the vent fauna of the Indian Ocean are not fully described yet, and its biodiversity is likely underestimated (Watanabe & Beedessee, 2015). Thus, the discovery of OVF can provide new insight to understanding faunal distributions and biogeographical relationships in the Indian Ocean.

Among the 21 macrofauna species collected at the OVF, six species were not yet described at the known active vent fields in the Indian Ocean (Table S1). Faunal composition of the OVF also shows variation from other Indian Ridge vent fauna. For example, some abundant species representing phylum in the CIR, including *Archinome jasoni* (Annelida), *Chrysomallon squamiferum* (scaly-foot gastropod), and *Phymorhynchus* sp. (Mollusca), were not found in the OVF. On the other hand, most Arthropoda including *Rimicaris kairei*, the most abundant animal found at the known vent fields of the Indian Ocean, *Mirocaris indica*, *Austinograea rodriguezensis*, *Munidopsis laticorpus*, and an endemic bivalve, *Bathymodiolus mariindicus*, were also found at the OVF.

A new vent mussel species sampled from the OVF was recently described and named *Gigantidas vrijenhoeki* n. sp (Jang et al., 2020). This is the first report of *Giantidas* mussels in the Indian Ocean. *Gigantidas* species also distributed in the Atlantic and western Pacific. Jang et al. (2020) showed that the *Gigantidas* species of the Atlantic exhibit a closer genetic relationship with some *Gigantidas* species of the western Pacific than to the OVF G. vrijenhoeki n. sp., which is another example against the "corridor" hypdothesis.

Cluster analysis of hydrothermal vent animals across six vent fields in the Indian Ocean shows similarity less than 40% between the OVF and other vent fields on the CIR (Figure 8). Although the analysis shows that the fauna at Dodo is most different from other vent fields, the data are limited since only four species were reported at the Dodo vent field.

Recently, interest in meiofauna inhabiting deep sea hydrothermal vents has been increasing, and several studies have been reported (Copley et al., 2007; Cuvelier et al., 2014; Degen et al., 2012; Gollner et al., 2013; Sarrazin et al., 2015; Zekely et al., 2006). Previous studies of meiofauna in hydrothermal vents were mostly conducted on the East Pacific Rise (EPR), the West Pacific (WP) back-arc basins, and the MAR (Vanreusel et al., 2010). Few investigations on meiofauna have been reported for the hydrothermal vents of the Indian Ocean. In the hydrothermal vents of the EPR, MAR, and WP, the dominant nematode is the Family Monhysteridae, genus *Thalassomonhystera*. However, nematodes collected from the OVF did not include Family Monhysteridae specimens. The most dominant nematode in this study, *Halalaimus* spp., is known as a species that is common in the nonvent field deep sea environment (Hauquier et al., 2019). As only one sediment sample for meiofauna was available from the OVF in this survey, further investigation is required to understand meiofauna composition in the OVF.

The OVF is located more than 800 km from previously known vent fields on the CIR, though the plume surveys of Son et al. (2014) suggest there are additional active sites on the MCIR segments south (12°S to 17°S) of Segment 3, and some may be very similar to OVF. Considering its isolated location, relatively shallow depth, and metal-poor/methane-rich vent fluid, the vent fauna of the OVF adds valuable information to understand the relatively unknown ecology and biogeography of Indian Ocean hydrothermal vents. Further investigation on faunal assemblages including new species, molecular analyses, and stable isotope composition of taxa in the OVF are required.

6. Conclusions

During the exploration for hydrothermal venting along the slow- to intermediate- spreading ridge segments of the CIR between 8°S and 12°S, four active hydrothermal vent fields have been confirmed by seafloor visual observation and sampling.

The Segment 1 hydrothermal vent field is located on the base of an OCC, <4 km from the spreading axis. Although only one diffusely venting chimney was observed by camera tows, the water column plume data (particle, ORP, Fe, Mn, and CH_4) indicate the likely presence of high-temperature venting at this site. The plume had a low CH_4/DMn value (~0.3), similar to those of basaltic-hosted systems despite its location on the slope of an OCC, so the heat source is likely magmatic (axial magma chamber or lateral dikes) and its location controlled by fluid pathways associated with tectonic extension and development of the OCC.

On Segment 2, two hydrothermal vent fields were located on axis-parallel abyssal hills, typical of symmetrical ridge sections at distances of 6 and 9 km from the ridge axis, respectively. Weak particle and ORP anomalies along with low dissolved metals and CH_4 concentrations in the plumes over each field are consistent with the low-temperature, diffuse venting detected during camera tows. Hydrothermal mineralization was primarily silica rich. The presence of vent fields as far as 9 km distant from the ridge axis is consistent with the expectation that widespread diffuse flow may be more common on ridge flanks than has been previously demonstrated and that crustal cooling by seawater infiltrates highly permeable off-axis fault zones. Our results that all newly discovered active vent fields in this study were located off-axis highlight the importance for future explorations on slow to intermediate spreading ridges with broad axial valleys to include off-axis flank areas in their surveys.

The OVF, with abundant vent animals, was discovered at the summit of OCC 3-2 on Segment 3 (OVF). Water column plumes from the OVF were characterized by a large ORP anomaly, high dissolved CH_4, and low dissolved metal concentrations with only very small or absent particle anomalies, consistent with low-temperature venting hosted by ultramafic rock. However, disseminated sulfide assemblages and secondary Cu minerals associated with hydrothermal precipitates suggested the hydrothermal system might be affected by lithospheric and/or magmatic heat as well as serpentinization. Among the identified 21 macrofaunal taxa, six species were not documented at previously known vent fields in the Indian Ocean. The isolated location and unique venting style of the OVF can provide valuable information toward understanding the ecology and biogeography of Indian Ocean hydrothermal vents.

Data Availability Statement

Bathymetric and water column data are available at the Mendeley Data repository (https://doi.org/10.17632/nm2sbbjx59.1).

References

American Public Health Association (1985). *Standard methods for the examination of water and wastewater* (16th ed.). Washington, DC: American Public Health Association.

Baker, E. T. (2009). Relationships between hydrothermal activity and axial magma chamber distribution, depth, and melt content. *Geochemistry, Geophysics, Geosystems*, *10*, Q06009. https://doi.org/10.1029/2009GC002424

Baker, E. T., Cormier, M., Langmuir, C. H., & Zavala, K. (2001). Hydrothermal plumes along segments of contrasting magmatic influence, 15°20′–18°30′N, East Pacific Rise: Influence of axial faulting. *Geochemistry, Geophysics, Geosystems*, *2*(9), 1051. https://doi.org/10.1029/2000GC000165

Baker, E. T., & German, C. R. (2004). On the global distribution of hydrothermal vent fields. In Mid-Ocean Ridges: Hydrothermal interactions between the lithosphere and oceans. In C. R. German, J. Lin, & L. M. Parson (Eds.), *Mid-Ocean Ridges: Hydrothermal interactions between lithosphere and oceans*, Geophysical Monograph Series (Vol. 148, pp. 245–266). Washington, DC: American Geophysical Union.

Baker, E. T., Hey, R. N., Lupton, J. E., Resing, J. A., Feely, R. A., Gharib, J. J., et al. (2002). Hydrothermal venting along Earth's fastest spreading center: East Pacific Rise, 27.5°–32.3°. *Journal of Geophysical Research*, *107*(B), 2130. https://doi.org/10.1029/2001JB000651

Baker, E. T., Martinez, F., Resing, J. A., Walker, S. L., Buck, N. J., & Edward, M. H. (2010). Hydrothermal cooling along the Eastern Lau Spreading Center: No evidence for discharge beyond the neovolcanic zone. *Geochemistry, Geophysics, Geosystems*, *11*, Q08004. https://doi.org/10.1029/2010GC003106

Baker, E. T., Resing, J. A., Haymon, R. M., Tunnicliffe, V., Lavelle, J. W., Martinez, F., et al. (2016). How many vent fields? New estimates of vent field populations on ocean ridges from precise mapping of hydrothermal discharge locations. *Earth and Planetary Science Letters*, *449*, 186–196. https://doi.org/10.1016/j.epsl.2016.05.031

Beaulieu, S., Baker, E. T., & German, C. R. (2015). Where are the undiscovered hydrothermal vents on oceanic spreading ridges? *Deep Sea Research, Part II*, *121*, 202–212. https://doi.org/10.1016/j.dsr2.2015.05.001

Beaulieu, S., Baker, E. T., German, C. R., & Maffei, A. (2013). An authoritative global database for active submarine hydrothermal vent fields. *Geochemistry, Geophysics, Geosystems*, *14*, 4892–4905. https://doi.org/10.1002/2013GC004998

Bogdanov, Y. A., Sagalevitch, A. M., Chernyaev, E. S., Ashadze, A. M., Gurvich, E. G., Lukashin, V. N., et al. (1995). A study of the hydrothermal field at 14°45′N on the Mid-Atlantic Ridge using the MIR submersibles. *Bridge Newsletter*, *9*, 9–13.

Boulart, C., Briais, A., Chavagnac, V., Révillon, S., Ceuleneer, G., Donval, J., et al. (2017). Contrasted hydrothermal activity along the South-East Indian Ridge (130°E–140°E): From crustal to ultramafic circulation. *Geochemistry, Geophysics, Geosystems*, *18*, 2446–2458. https://doi.org/10.1002/2016GC006683

Burgess, R. (2001). An improved protocol for separating meiofauna from sediments using colloidal sols. *Marine Ecology Progress Series*, *214*, 161–165. https://doi:10.3354/meps214161

Charlou, J. L., Donval, J. P., Fouquet, Y., Jean-Baptiste, P., & Holm, N. (2002). Geochemistry of high H_2 and CH_4 vent fluids issuing from ultramafic rocks at the Rainbow hydrothermal field (36°14′N, MAR). *Chemical Geology*, *191*(4), 345–359. https://doi.org/10.1016/S0009-2541(02)00134-1

Connelly, D. P., Copley, J. T., Murton, B. J., Stansfield, K., Tyler, P. A., German, C. R., et al. (2012). Hydrothermal vent fields and chemosynthetic biota on the world's deepest seafloor spreading centre. *Nature Communications*, *3*(1), 620. doi, https://doi.org/10.1038/ncomms1636

Copley, J. T., Marsh, L., Glover, A. G., Hühnerbach, V., Nye, V. E., Reid, W. D. K., et al. (2016). Ecology and biogeography of megafauna and macrofauna at the first known deep-sea hydrothermal vents on the ultraslow-spreading Southwest Indian Ridge. *Scientific Reports*, *6*(1), 39,158. https://doi.org/10.1038/srep39158

Copley, J. T. P., Flint, H. C., Ferrero, T. J., & Van Dover, C. L. (2007). Diversity of meiofauna and free-living nematodes in hydrothermal vent mussel beds on the northern and southern East Pacific Rise. *Journal of the Marine Biological Association of the United Kingdom*, *87*(5), 1141–1152. https://doi.org/10.1017/s0025315407055956

Cuvelier, D., Beesau, J., Ivanenko, V. N., Zeppilli, D., Sarradin, P. M., & Sarrazin, J. (2014). First insights into macro- and meiofaunal colonisation patterns on paired wood/slate substrata at Atlantic deep-sea hydrothermal vents. *Deep Sea Research Part I*, *87*, 70–81. https://doi.org/10.1016/j.dsr.2014.02.008

Degen, R., Riavitz, L., Gollner, S., Vanreusel, A., Plum, C., & Bright, M. (2012). Community study of tubeworm-associated epizooic meiobenthos from deep-sea cold seeps and hot vents. *Marine Ecology Progress Series*, *468*, 135–148. https://doi.org/10.3354/meps09889

Desbruyères, D., Hashimoto, J., & Fabri, M.-C. (2007). Composition and biogeography of hydrothermal vent communities in western Pacific back-arc basins. In D. M. Christie, C. R. Fisher, S.-M. Lee, & S. Givens (Eds.), *Back-arc spreading systems: Geological, biological, chemical, and physical interactions*, *Geophysical Monograph Series* (Vol. 166, pp. 215–234). Washington, DC: American Geophysical Union.

Edmond, J. M., Measures, C., McDuff, R. E., Chan, L. H., Collier, R., Grant, B., et al. (1979). Ridge crest hydrothermal activity and the balances of the major and minor elements in the ocean: The Galapagos data. *Earth and Planetary Science Letters*, *46*(1), 1–18. https://doi.org/10.1016/0012-821x(79)90061-x

Fouquet, Y., Cambon, P., Etoubleau, J., Charlou, J. L., Ondreas, H., Barriga, F. J. A. S., et al. (2010). Geodiversity of hydrothermal processes along the Mid-Atlantic Ridge and ultramafic-hosted mineralization: A new type of oceanic Cu-Zn-Co-Au volcanogenic massive sulfide deposit. In P. A. Rona, et al. (Eds.), *Diversity of hydrothermal systems on slow spreading ocean ridges*, *Geophysical Monograph Series* (Vol. 188, pp. 321–367). Washington, DC: American Geophysical Union. https://doi.org/10.1029/2008GM000746

Fouquet, Y., Ondréas, H., Charlou, J.-L., Donval, J. -P., Radford-Knoery, J., Costa, I., et al. (1995). Atlantic lava lakes and hot vents. *Nature*, *377*(6546), 201. https://doi.org/10.1038/377201a0

Gallant, R. M., & Von Damm, K. L. (2006). Geochemical controls on hydrothermal fluids from the Kairei and Edmond Vent Fields, 23°–25°S, Central Indian Ridge. *Geochemistry, Geophysics, Geosystems*, *7*, Q06018. https://doi.org/10.1029/2005GC001067

Gamo, T., Chiba, H., Yamanaka, T., Okudaira, T., Hashimoto, J., Tsuchida, S., et al. (2001). Chemical characteristics of newly discovered black smoker fluids and associated hydrothermal plumes at the Rodriguez Triple Junction, Central Indian Ridge. *Earth and Planetary Science Letters*, *193*(3-4), 371–379. https://doi.org/10.1016/s0012-821x(01)00511-8

Gente, P., Mevel, C., Auzende, J. M., Karson, J. A., & Fouquet, Y. (1991). An example of a recent accretion on the Mid-Atlantic Ridge: The Snake Pit neovolcanic ridge (MARK area, 23°22′N). *Tectonophysics*, *190*(1), 1–29. https://doi.org/10.1016/0040-1951(91)90352-S

German, C. R., Baker, E. T., Mevel, C., Tamaki, K., & the FUJI Scientific Team (1998). Hydrothermal activity along the Southwest Indian Ridge. *Nature*, *395*(6701), 490–493. https://doi.org/10.1038/26730

German, C. R., Bennet, S. A., Connelly, D. P., Evans, A. J., Murton, B. J., Parson, L. M., et al. (2008). Hydrothermal activity on the southern Mid-Atlantic Ridge: Tectonically- and volcanically-controlled venting at 4–5°S. *Earth and Planetary Science Letters*, *273*(3-4), 332–344. https://doi.org/10.1016/j.epsl.2008.06.048

German, C. R., Bowen, A., Coleman, M. L., Honig, D. L., Huber, J. A., Jakuba, M. V., et al. (2010). Diverse styles of submarine venting on the ultraslow spreading Mid-Cayman Rise. *Proceedings of the National Academy of Sciences of the United States of America*, *107*(32), 14020–14025. https://doi.org/10.1073/pnas.1009205107

German, C. R., & Seyfried, W. E. Jr. (2014). Hydrothermal processes. In H. D. Holland, & K. K. Turekian (Eds.), *Treatise on Geochemistry* (2nd ed., Vol. 8, pp. 191–233). Oxford, U. K: Elsevier.

Gharib, J. J., Sansone, F. J., Resing, J. A., Baker, E. T., Lupton, J. E., & Massoth, G. J. (2005). Methane dynamics in hydrothermal plumes over a superfast spreading center: East Pacific Rise, 27.5°–32.3°S. *Journal of Geophysical Research*, *110*, B10101. https://doi.org/10.1029/2004JB003531

Gollner, S., Miljutina, M., & Bright, M. (2013). Nematode succession at deep-sea hydrothermal vents after a recent volcanic eruption with the description of two dominant species. *Organisms, Diversity and Evolution*, *13*(3), 349–371. https://doi.org/10.1007/s13127-012-0122-2

Harding, J. L., Van Avendonk, H. J. A., Hayman, N. W., Grevemeyer, I., Peirce, C., & Dannowski, A. (2017). Magmatic-tectonic conditions for hydrothermal venting on an ultraslow-spread oceanic core complex. *Geology*, *45*(9), 839–842. https://doi.org/10.1130/G39045.1

Hauquier, F., Macheriotou, L., Bezerra, T. N., Egho, G., Martínez Arbizu, P., & Vanreusel, A. (2019). Distribution of free-living marine nematodes in the Clarion-Clipperton Zone: Implications for future deep-sea mining scenarios. *Biogeosciences*, *16*(18), 3475–3489. https://doi.org/10.5194/bg-16-3475-2019

Hodgkinson, M. R., Webber, A. P., Roberts, S., Mills, R. A., Connelly, D. P., & Murton, B. J. (2015). Talc-dominated seafloor deposits reveal a new class of hydrothermal system. *Nature Communications*, *6*(1), 10,150. https://doi.org/10.1038/ncomms10150

Humphris, S. E., Zierenberg, R. A., Mullineaux, L. S., & Thomson, R. E. (Eds) (1995). *Seafloor hydrothermal systems: Physical, chemical, biological, and geological interactions*, *Geophysical Monograph Series* (Vol. 97). Washington DC: American Geophysical Union. https://doi.org/10.1029/GM091

Jang, S., Ho, P., Jun, S., Kim, D., & Won, Y. (2020). A newly discovered *Gigantidas* bivalve mussel from the Onnuri Vent Field in the northern Central Indian Ridge. *Deep Sea Research, Part I*, *161*, 103299. https://doi.org/10.1016/J.dsr.2020.103299

Kawagucci, S., Miyazaki, J., Noguchi, T., Okamura, K., Shibuya, T., Watsuji, T., et al. (2016). Fluid chemistry in the Solitaire and Dodo hydrothermal fields of the Central Indian Ridge. *Geofluids*, *16*(5), 988–1005. https://doi.org/10.1111/gfl.12201

Kawagucci, S., Okamura, K., Kiyota, K., Tsunogai, U., Sano, Y., Tamaki, K., & Gamo, T. (2008). Methane, manganese, and helium-3 in newly discovered hydrothermal plumes over the Central Indian Ridge, 18°–20°S. *Geochemistry, Geophysics, Geosystems*, *9*, Q10002. https://doi.org/10.1029/2008GC002082

Kelley, D. S., Karson, J. A., Früh-Green, G. L., Yoerger, D. R., Shank, T. M., Butterfield, D. A., et al. (2005). A serpentinite-hosted submarine ecosystem: The Lost City hydrothermal field. *Science*, *307*(5714), 1428–1434. https://doi.org/10.1126/science.1102556

Kumagai, H., Nakamura, K., Toki, T., Morishita, T., Okino, K., Ishibashi, J.-I., et al. (2008). Geological background of the Kairei and Edmond hydrothermal fields along the Central Indian Ridge: Implications of their vent fluids' distinct chemistry. *Geofluids*, *8*(4), 239–251. https://doi.org/10.1111/j.1468-8123.2008.00223.x

McCaig, A. M., Cliff, R. A., Escartín, J., Fallick, A., & MacLeod, C. J. (2007). Oceanic detachment faults focus very large volumes of black smoker fluids. *Geology*, *35*(10), 935–938. https://doi.org/10.1130/G23657A.1

Melchert, B., Devey, C. W., German, C. R., Lackschewitz, K. S., Seifert, R., Walter, M., et al. (2008). First evidence for high-temperature off axis venting of deep crustal/mantle heat: The Nibelungen hydrothermal field, southern Mid-Atlantic Ridge. *Earth and Planetary Science Letters*, *275*(1-2), 61–69. https://doi.org/10.1016/j.epsl.2008.08.010

Nakamura, K., Watanebe, H., Miyazaki, J., Takai, K., Kawagucci, S., Noguchi, T., et al. (2012). Discovery of new hydrothermal activity and chemosynthetic fauna on the Central Indian Ridge at 18°–20°S. *PLoS ONE*, *7*(3), e32965. https://doi.org/10.1371/journal.pone.0032965

Ohta, K., Terai, H., Kimura, I., & Tanaka, K. (1999). Simultaneous determination of hydrogen, methane, and carbon monoxide in water by gas chromatography with a semiconductor detector. *Analytical Chemistry*, *71*(14), 2697–2699. https://doi.org/10.1021/ac981452l

Okino, K., Nakamura, K., & Sato, H. (2015). Tectonic background of four hydrothermal fields along the Central Indian Ridge. In J. Ishibashi, K. Okino, & M. Sunamura (Eds.), *Subseafloor biosphere linked to hydrothermal systems: TAIGA concept* (pp. 133–146). Springer: Tokyo.

Pak, S. J., Moon, J. W., Kim, J., Chandler, M. T., Kim, H. S., Son, J., et al. (2017). Widespread tectonic extension at the Central Indian Ridge between 8°S and 18°S. *Gondwana Research*, *45*, 163–179. https://doi.org/10.1016/j.gr.2016.12.015

Platt, H. M., & Warwick, R. M. (1983). *Free-living marine nematodes. Part I. British Enoplids*. Cambridge: the Linnean Society of London and the estuarine and brackish-water sciences association.

Platt, H. M., & Warwick, R. M. (1988). *Free-living marine nematodes. Part II. British Chromadorids*. Leiden: The Linnean Society of London and The Estuarine and Brackishwater Sciences Association.

Rona, P. A., Klinkhammer, G., Nelsen, T. A., Trefry, J. H., & Elderfield, H. (1986). Black smokers, massive sulfides, and vent biota at the Mid-Atlantic Ridge. *Nature*, *321*(6065), 33–37. https://doi.org/10.1038/321033a0

Sarrazin, J., Legendre, P., De Busserolles, F., Fabri, M. C., Guilini, K., Ivanenko, V. N., et al. (2015). Biodiversity patterns, environmental drivers and indicator species on a high temperature hydrothermal edifice, Mid-Atlantic Ridge. *Deep Sea Research Part II*, *121*, 177–192. https://doi.org/10.1016/j.dsr2.2015.04.013

Schmidt, K., Koschinsky, A., Garbe-Schönberg, D., De Carvalho, L. M., & Seifert, R. (2007). Geochemistry of hydrothermal fluids from the ultramafic-hosted Logatchev hydrothermal field, 15°N on the Mid-Atlantic Ridge: Temporal and spatial investigation. *Chemical Geology*, *242*(1-2), 1–21. https://doi.org/10.1016/j.chemgeo.2007.01.023

Shank, T. M. (2004). The evolutionary puzzle of seafloor life. *Oceanus*, *42*(2), 78–85.

Son, J., Pak, S. J., Kim, J., Baker, E. T., You, O. R., Son, S. K., & Moon, J. W. (2014). Tectonic and magmatic control of hydrothermal activity along the slow-spreading Central Indian Ridge, 8°S–17°S. *Geochemistry, Geophysics, Geosystems*, *15*, 2011–2020. https://doi.org/10.1002/2013GC005206

Tao, C., Lin, J., Guo, S., Chen, Y. J., Wu, G., Han, X., et al. (2012). First active hydrothermal vents on an ultraslow-spreading center: Southwest Indian Ridge. *Geology*, *40*(1), 47–50. https://doi.org/10.1130/G32389.1

Tucholke, B. E., Lin, J., & Kleinrock, M. C. (1998). Megamullions and mullion structure defining oceanic metamorphic core complexes on the Mid-Atlantic Ridge. *Journal of Geophysical Research*, *103*(B5), 9857–9866. https://doi.org/10.1029/98JB00167

Van Dover, C. L., German, C. R., Speer, K. G., Parson, L. M., & Vrijenhoek, R. C. (2002). Evolution and biodiversity of deep-sea vent and seep invertebrates. *Science*, *295*(5558), 1253–1257. https://doi.org/10.1126/science.1067361

Van Dover, C. L., Humphris, S. E., Fornari, D., Cavanaugh, C. M., Collier, R., Goffredi, S. K., et al. (2001). Biogeography and ecological setting of Indian Ocean hydrothermal vents. *Science*, *294*(5543), 818–823. https://doi.org/10.1126/science.1064574

Vanreusel, A., De Groote, A., Gollner, S., & Bright, M. (2010). Ecology and biogeography of free-living nematodes associated with chemosynthetic environments in the deep sea: A review. *PLoS ONE*, *5*(8), e12449. https://doi.org/10.1371/journal.pone.0012449

Von Damm, K. L. (1990). Seafloor hydrothermal activity black smoker chemistry and chimneys. *Annual Review of Earth and Planetary Sciences*, *18*(1), 173–204. https://doi.org/10.1146/annurev.earth.18.1.173

Walker, S. L., Baker, E. T., Resing, J. A., Nakamura, K. & McLain, P. D. (2007). A new tool for detecting hydrothermal plumes: An ORP sensor for the PMEL MAPR, *Eos Trans. AGU, 88*(52), Fall Meet. Suppl., Abstract V21D-0753.

Warwick, R. M., Platt, H. M., & Somerfield, P. J. (1998). *Free-living marine nematodes. Part III. British monohysterids. Synopsis of British fauna (new series) No. 53*. Shrewsbury: Field Studies Council.

Watanabe, H., & Beedessee, G. (2015). Vent fauna on the Central Indian Ridge. In J. Ishibashi, K. Okino, & M. Sunamura (Eds.), *Subseafloor biosphere linked to hydrothermal systems: TAIGA concept* (pp. 205–212). Springer: Tokyo.

Watanabe, H. K., Chen, C., Marie, D. P., Takai, K., Fujikura, K., & Chan, B. K. K. (2018). Phylogeography of hydrothermal vent stalked barnacles: A new species fills a gap in the Indian Ocean "disperal corridor" hypothesis. *Royal Society Open Science*, *5*(4), 172408. https://doi.org/10.1098/rsos.172408

Wheeler, A. J., Murton, B., Copley, J., Lim, A., Carlsson, J., Collins, P., et al. (2013). Moytirra: Discovery of the first known deep-sea hydrothermal vent field on the slow-spreading Mid-Atlantic Ridge north of the Azores. *Geochemistry, Geophysics, Geosystems*, *14*, 4170–4184. https://doi.org/10.1002/ggge.20243

Yi, S. B., Oh, C. W., Pak, S. J., Kim, J., & Moon, J. W. (2014). Geochemistry and petrogenesis of mafic-ultramafic rocks from the Central Indian Ridge, latitude 8°–17°S: Denudation of mantle harzburgites and gabbroic rocks and compositional variation of basalts. *International Geology Review*, *56*(14), 1691–1719. https://doi.org/10.1080/00206814.2014.955539

Zekely, J., Gollner, S., Van Dover, C. L., Govenar, B., Le Bris, N., Nemeschkal, H., & Bright, M. (2006). Nematode communities associated with tube worm and mussel aggregations on the East Pacific Rise. *Cahiers de Biologie Marine*, *47*, 477–482.